

# Contents

<b>1</b>	<b>The Standard Model and beyond</b>	<b>3</b>
1.1	The Standard Model . . . . .	3
1.1.1	Fundamental Particles . . . . .	3
1.1.2	Gauge Symmetries . . . . .	4
1.1.3	Spontaneous Symmetry Breaking and the Higgs Boson . . . . .	9
1.2	The Higgs boson . . . . .	14
1.2.1	The Higgs boson: production mechanisms . . . . .	14
1.2.2	The Higgs boson: decay channels . . . . .	16
1.3	Beyond Standard Model (BSM) . . . . .	16
<b>2</b>	<b>The CMS detector at LHC</b>	<b>19</b>
2.1	The Large Hadron Collider . . . . .	19
2.2	The Compact Muon Solenoid . . . . .	21
2.2.1	The tracking system . . . . .	23
2.2.2	Electromagnetic calorimeter . . . . .	26
2.2.3	Hadronic Calorimeter . . . . .	28
2.3	Magnet . . . . .	31
2.4	Muon System . . . . .	32
2.5	Trigger and Data Acquisition . . . . .	37
2.5.1	Level 1 Trigger . . . . .	38
<b>3</b>	<b>Object reconstruction in CMS</b>	<b>41</b>
3.1	Photons . . . . .	41
3.2	Electrons . . . . .	42
	<b>Bibliography</b>	<b>44</b>



# Chapter 1

## The Standard Model and beyond

Particle Physics studies the building blocks of the matter, the so called fundamental particle, and how they are governed by the four fundamental forces<sup>1</sup>.

The best theory, explaining our understanding of these particles and forces, is the *Standard Model* (SM): developed during the 1970s, it has successfully explained almost all experimental results and precisely predicted a wide variety of physical phenomena. This chapter will describe in details the Standard Model and some theories developed in order to solve some unanswered questions.

### 1.1 The Standard Model

#### 1.1.1 Fundamental Particles

All matter around us is made of elementary particles with no substructure, well defined by some quantum numbers. These particles are divided into two groups: *leptons*, with an entire value of electric charge, and *quarks*, with a fractional charge. Each group consists of six particles, which are related in pairs or generations. The six quarks are paired in the three generations: the up and the down quark form the first generation (u, d), followed by the charm and strange (c, s), then the top and bottom (or beauty) quark (t, b). The six leptons are also similarly arranged in three generations: the electron (e) and the electronic neutrino ( $\nu_e$ ), the muon ( $\mu$ ) with the muonic neutrino ( $\nu_\mu$ ), and the tau ( $\tau$ ) with the tauonic neutrino ( $\nu_\tau$ ). While electron, muon and tau are charged particles, the neutrinos are electrically neutral. In Table 1.1 and 1.2, the features of leptons and quarks.

Beside leptons and quarks, there are other particles called *bosons* responsible of carrying (or mediating) the fundamental forces:. Electromagnetic Force, responsible of all electrical and magnetic phenomena, is mediated by the photons  $\gamma$ ; the Weak Force, responsible of some decays, is mediated by  $W^\pm$  and  $Z$  bosons; the Strong Force, responsible for example of the atomic structure, is mediated by the gluons ( $g$ ). Last

---

<sup>1</sup>In the thesis, Natural Units will be used:  $c = \hbar = 1$ , where  $\hbar = h/2\pi = 6.58211889(26) \cdot 10^{-23} MeVs$  and  $c = 299792458 ms^{-1}$ .

Leptons		
Flavor	Charge	Mass[MeV]
electronic neutrino ( $\nu_e$ )	0	$< 0.002$
electron ( $e$ )	-1	0.511
muonic neutrino ( $\nu_\mu$ )	0	$< 0.19$
muon ( $\mu$ )	-1	105.66
tauonic neutrino ( $\nu_\tau$ )	0	$< 18.2$
tau ( $\tau$ )	-1	$1776.86 \pm 0.12$

Table 1.1: Standard Model leptons features [1].

Quark		
Flavor	Carica	Massa[GeV]
up ( $u$ )	+2/3	$0.0022^{+0.0006}_{-0.0004}$
down ( $d$ )	-1/3	$0.0047^{+0.0005}_{-0.0004}$
charm ( $c$ )	+2/3	$1.28 \pm 3$
strange ( $s$ )	-1/3	$0.096 \pm 0.084$
top ( $t$ )	+2/3	$173.1 \pm 0.6$
bottom ( $b$ )	-1/3	$4.18^{+0.04}_{-0.03}$

Table 1.2: Standard Model quarks features [1].

fundamental force, but not yet included in the SM due to its low strength compared to the others, is the Gravity that is the weakest. In Table 1.3 the features of the bosons.

Bosons	Interaction	Charge	Mass[GeV]
photon ( $\gamma$ )	Electromagnetic	0	0
$W^\pm$	Weak	$\pm 1$	$80.385 \pm 0.015$
$Z^0$	Weak	0	$91.1876 \pm 0.0021$
gluoni	Strong	0	0

Table 1.3: Standard Model bosons features [1].

### 1.1.2 Gauge Symmetries

The present belief is that all particles interactions may be dictated by the so called *local gauge symmetries* and this is connected with the idea that the conserved physical quantities (such as electric charge) are conserved in local regions of space and not just globally[2].

The fundamental quantity in classical mechanics is the action  $S$ , the time integral of the Lagrangian  $L$ :

$$S = \int L dt = \int \mathcal{L}(\phi, \partial\phi/\partial x_\mu) d^4x \quad (1.1)$$

where  $\mathcal{L}$  is the Lagrangian Density<sup>2</sup> and  $\phi$  is the field, itself a function of the continuous parameters  $x_\mu$  [3][4].

$$L \equiv T - V \quad (1.2)$$

where  $T$  and  $V$  are the kinetic and potential energy of the system respectively.

Thanks to the *Principle of least action*<sup>3</sup> is possible deduce the *Euler-Lagrange* equations (1.3) from which can be obtained the particle equations of motion.

$$\frac{\partial \mathcal{L}}{\partial \phi} - \frac{\partial}{\partial x_\mu} \frac{\partial \mathcal{L}}{\partial (\partial\phi/\partial x_\mu)} = 0 \quad (1.3)$$

## QED

The interaction of electron with photon is described by the Quantum Electrodynamics. Let's start with a complex field  $\psi$  describing a free electron with mass  $m$ : its Lagrangian is

$$\mathcal{L} = \bar{\psi}(i\gamma^\mu \partial_\mu - m)\psi \quad (1.4)$$

and its equation of motion can be deduced by the Dirac Equation, obtained substituting 1.4 in 1.3.

The electromagnetic (em) field instead is described by the four-vector gauge potential  $A_\mu$ . The field strength tensor is defined as:

$$F_{\mu\nu} = \partial_\mu A_\nu - \partial_\nu A_\mu \quad (1.5)$$

and the equation of motion, in presence of an external current  $J^\mu$  is:

$$\partial_\mu F^{\mu\nu} = QeJ^\nu \quad (1.6)$$

In case now the electron interacts with the em field, the new Lagrangian is:

$$\mathcal{L}_{EM} = \bar{\psi}(i\gamma^\mu D_\mu - m)\psi - \frac{1}{4}F_{\mu\nu}F^{\mu\nu} \quad (1.7)$$

where  $D_\mu$ , known as covariant derivative, is defined as

$$D_\mu = \partial_\mu + ieQA_\mu \quad (1.8)$$

and the last term in 1.7 stands for Maxwell's equation.

It can be shown that 1.7 is invariant under the phase transformation:

$$\psi(x) \rightarrow e^{-iQ\theta}\psi(x) \quad (1.9)$$

---

<sup>2</sup>however, following standard use in field theory, we will often refer to  $\mathcal{L}$  simply Lagrangian.

<sup>3</sup>Fixed the values of the coordinates at the initial and at the final time, classical trajectory which satisfies these conditions is an extremum of the action.

with  $\theta \in \mathbb{R}$ . This transformation belongs to the group U(1) and according to Noether's theorem, it implies the existence of a conserved current: in this case, the electric charge. Since once the value of  $\theta$  is fixed, the invariance is specified for all space and time, it is known as *global gauge invariance*.

More interesting is the case in which the parameter  $\theta$  depends on space and time in a completely arbitrary way:

$$\psi(x) \rightarrow e^{-iQ\theta(x)}\psi(x) \quad (1.10)$$

and the Lagrangian 1.7 is not invariant. It can be shown that, in order to restore the Lagrangian invariance, the potential  $A_\mu$  must satisfy following condition:

$$A_\mu \rightarrow A_\mu + \frac{1}{e}\partial_\mu\theta \quad (1.11)$$

Under 1.10 and 1.11 the Lagrangian 1.7 is invariant.

One can observe the absent of mass term in the Lagrangian: this means that the boson associated to the potential  $A_\mu$ , the photon, must be massless: the presence of a mass term would make the Lagrangian not invariant under gauge transformation.

## QCD

The interaction between quarks and gluons is described by the Quantum Chromodynamics.

For quarks [5], it must be considered a new quantum number, the colour, such that each species of quark may have three different colours:  $q_j$ ,  $j = 1, 2, 3$  (red, green, blue). In order to avoid the existence of non-observed extra states with non-zero colour, one needs to further postulate that all asymptotic states are colourless, i.e. singlets under rotations in colour space. This assumption is known as the confinement hypothesis, because it implies the non-observability of free quarks: since quarks carry colour they are confined within colour-singlet bound states.

For free quark described by the field  $q_j$ , the Lagrangian is:

$$\mathcal{L} = \bar{q}_j(i\gamma^\mu\partial_\mu - m)q_j \quad (1.12)$$

In order to describe the interaction between quarks and gluons, it is needed to change the quark derivative by covariant objects. Since there are now eight independent gauge parameters, eight different gauge bosons  $G_a^\mu(x)$ , the so-called gluons, are needed:

$$D_{q_j}^\mu \equiv [\partial^\mu - ig_s \frac{\lambda^a}{2} G_a^\mu(x)] \quad (1.13)$$

The corresponding field strengths are also introduced:

$$G_a^{\mu\nu} = \partial^\mu G_a^\nu - \partial^\nu G_a^\mu + g_s f^{abc} G_b^\mu G_c^\nu \quad (1.14)$$

where  $g_s$  is the constant coupling. Hence, in case of interaction the new Lagrangian is:

$$\mathcal{L}_{QCD} = \bar{q}_j(i\gamma^\mu D_\mu - m)q_j - \frac{1}{4} G_a^{\mu\nu} G_a^{\mu\nu} \quad (1.15)$$

It can be shown 1.15 in invariant under arbitrary global  $SU(3)_C$  transformations in colour space 1.16:

$$q(x) \rightarrow q'(x) = Uq(x) \equiv e^{i\theta_a T^a} q(x), \quad a = 1, 2, \dots, 8 \quad (1.16)$$

where  $T_a$  are the generators of the SU(3) ( $n = N^2 - 1 = 3^2 - 1 = 8$ ) group linked with the  $\lambda_a$  Gell-Mann matrices.

More interesting is the case in which  $\theta$  depends on local coordinates,  $\theta_a = \theta_a(x)$ :

$$q(x) \rightarrow q'(x) = Uq(x) \equiv e^{i\theta_a(x) \frac{\lambda^a}{2}} q(x), \quad a = 1, 2, \dots, 8 \quad (1.17)$$

The group is non-Abelian since not all the generators  $\lambda_a$  commute with each other.

To ensure the invariance of the Lagrangian 1.15, the gauge fields must transform as follow:

$$G_{\mu a} \rightarrow G_{\mu a} - \frac{1}{g_s} \partial_\mu \theta_a - f_{abc} \theta^b G_\mu^c \quad (1.18)$$

The field tensor  $G_a^{\mu\nu}$  has a remarkable new property: imposing gauge symmetry (1.17 and 1.18), it has required kinematic energy term in 1.15 is not purely kinetic but includes an induced self-interaction between the gauge bosons. Decomposing the Lagrangian into its different pieces, there are three terms analogues to QED describing the free propagation of quarks and gluons and the quark-gluon interaction and two terms showing the presence of three and four gluon self-coupling in QCD reflecting the fact that gluons themselves carry color charge. They have no analogue in QED and arise on account of the non-Abelian character of the gauge group. As in QED, the absence of a mass term implies gluons must be massless.

### The electroweak theory

Low-energy experiments have provided a large amount of information about the dynamics underlying flavour-changing processes. The detailed analysis of the energy and angular distributions in  $\beta$  decays, such as  $\mu^- \rightarrow e^- \bar{\nu}_e \nu_\mu$ , made clear that only the left-handed (right-handed) fermion (antifermion) chiralities participate in those weak transitions. Moreover, the strength of the interaction appears to be universal.

Using gauge invariance, it is possible to determine the right QED (1.7) and QCD (1.15) Lagrangians. To describe weak interactions, a more elaborated structure is needed, with several fermionic flavours and different properties for left- and right-handed fields. Moreover, the left-handed fermions should appear in doublets, and we would like to have gauge bosons in addition to the photon. The simplest group with doublet representations is SU(2) while to include also the electromagnetic interactions an additional U(1) group is needed. The obvious symmetry group to consider is then:

$$G \equiv SU(2)_L \otimes U(1)_Y \quad (1.19)$$

where L refers to left-handed fields and Y stands for the weak hypercharge.  
Let's consider a single family of leptons:

$$\chi_L = \begin{pmatrix} \nu_l \\ l^- \end{pmatrix}_L, \quad \psi_R = l_R^- \quad (1.20)$$

or for quarks

$$\chi_L = \begin{pmatrix} u \\ d \end{pmatrix}_L, \quad \psi_R = u_R, \text{ or } d_R \quad (1.21)$$

As in QED and QCD case, starts with free Lagrangian:

$$\mathcal{L} = i\bar{\chi}_L \gamma^\mu \partial_\mu \chi_L + i\bar{\psi}_R \gamma^\mu \partial_\mu \psi_R \quad (1.22)$$

The interaction is again introduced changing the derivative with the covariant:

$$D_\mu = \partial_\mu + igW_\mu^a T_a + ig' B_\mu Y \quad (1.23)$$

where  $W_\mu^a$   $a = 1, 2, 3$  are the three gauge bosons associated with the group  $SU(2)_L$ ,  $T^a$  its generators and g the constant couplings;  $B_\mu$ , Y and g are instead respectively the gauge boson, the generator and the constant coupling for the group  $U(1)_Y$ . With  $W_\mu^a$  and  $B_\mu$  can be introduced also the tensor strength fields:

$$\begin{aligned} W_a^{\mu\nu} &= \partial^\mu W_a^\nu - \partial^\nu W_a^\mu + g\epsilon^{abc} W_b^\mu W_c^\nu \\ B^{\mu\nu} &= \partial^\mu B^\nu - \partial^\nu B^\mu \end{aligned} \quad (1.24)$$

Therefore, the properly Lagrangian is given by:

$$\mathcal{L} = i\bar{\chi}_L \gamma^\mu D_\mu \chi_L + i\bar{\psi}_R \gamma^\mu D_\mu \psi_R - \frac{1}{4} B_{\mu\nu} B^{\mu\nu} - \frac{1}{4} W_{\mu\nu} W^{\mu\nu} \quad (1.25)$$

In 1.25  $W_{\mu\nu} = W_{\mu\nu}^a \sigma^a / 2$  with  $\sigma^a$  2x2 Pauli's matries.

As in QED and QCD case, also electroweak interaction is invariant under global transformation:

$$\begin{aligned} \chi_L &\rightarrow \chi'_L = e^{i\alpha_a T^a + i\beta Y} \chi_L \\ \psi_R &\rightarrow \psi'_R = e^{i\beta Y} \psi_R \end{aligned} \quad (1.26)$$

Moving to local transformation, in order to guarantee Lagrangian 1.25 to be invariant, the gauge bosons must have following transformation rules:

$$\begin{aligned} W_\mu^a &\rightarrow U_L(x) W_\mu^a U_L(x)^\dagger - \frac{i}{g} \partial_\mu U_L(x) U_L(x)^\dagger, \\ B_\mu &\rightarrow B_\mu + \frac{1}{g'} \partial_\mu \beta \end{aligned} \quad (1.27)$$

where  $U(x)_L = e^{i\sigma_a/2 \alpha(x)^a}$ . The transformation of  $B_\mu$  is identical to the one obtained in QED for the photon, while the  $SU(2)_L$   $W_\mu^a$  fields transform in analogous way to the gluon fields of QCD.

The gauge symmetry forbids to write a mass term for the gauge bosons in 1.25. Fermionic masses are also not possible, because they would communicate the left- and right-handed fields, which have different transformation properties, and therefore would produce an explicit breaking of the gauge symmetry. Thus, the  $SU(2)_L \otimes U(1)_Y$  Lagrangian in 1.25 only contains massless fields.

The term containing the  $SU(2)_L$  matrix:

$$\frac{\sigma_a}{2} W_\mu^a = \frac{1}{\sqrt{2}} \begin{pmatrix} \sqrt{2}W_\mu^3 & W_\mu^+ \\ W_\mu^- & -\sqrt{2}W_\mu^3 \end{pmatrix} \quad (1.28)$$

gives rise to charged-current interactions with the bosons field  $W_\mu^\pm \equiv (W_\mu^1 \mp iW_\mu^2)/\sqrt{2}$ . La Lagrangian 1.25 contains also interactions with the neutral gauge field  $W_\mu^3$  and  $B_\mu$ ; one can define

$$Z_\mu = \frac{gW_\mu^3 - g'B_\mu}{\sqrt{g^2 + g'^2}}, \quad A_\mu = \frac{gW_\mu^3 + g'B_\mu}{\sqrt{g^2 + g'^2}} \quad (1.29)$$

and thinking them as a rotation, introducing the Weinberg angle  $\theta_W$  so that  $\cos \theta_W = g/\sqrt{g^2 + g'^2}$  (and  $\sin \theta_W = g'/\sqrt{g^2 + g'^2}$ ):

$$Z_\mu = \cos \theta_W W_\mu^3 - \sin \theta_W B_\mu, \quad A_\mu = \sin \theta_W W_\mu^3 + \cos \theta_W B_\mu \quad (1.30)$$

or reversing:

$$\begin{pmatrix} W_\mu^3 \\ B_\mu \end{pmatrix} \equiv \begin{pmatrix} \cos \theta_W & \sin \theta_W \\ -\sin \theta_W & \cos \theta_W \end{pmatrix} \begin{pmatrix} Z_\mu \\ A_\mu \end{pmatrix} \quad (1.31)$$

With these definitions, it can be observed the  $A_\mu$  in 1.25 couple in the same way with  $l_L$  and  $l_R$  as the photon: to get QED from these one needs to impose

$$g \sin \theta_W = g' \cos \theta_W = e \quad (1.32)$$

At the same time,  $Z_\mu$ , can be identify with the Z boson, mediator of the Weak Interaction.

Once again, no mass term is present in 1.25 and this means that  $W^\pm$  and Z must be massless: this is in contrast with experimental evidence [6][7].

The way to generate the mass of the particle is through the so called *Spontaneous Symmetry Breaking* (SSB): this mechanism appear in those cases where one has a symmetric Lagrangian, but a non-symmetric vacuum.

### 1.1.3 Spontaneous Symmetry Breaking and the Higgs Boson

Let's consider a complex scalar field  $\phi(x) = (\phi_1 + \phi_2)/\sqrt{2}$ , with Lagrangian:

$$\mathcal{L} \equiv T - V = (\partial_\mu \phi)^*(\partial^\mu \phi) - \mu^2(\phi^* \phi) - \lambda(\phi^* \phi)^2 \quad (1.33)$$

1.33 is invariant under global phase transformation of the scalar field (it possesses a U(1) global gauge symmetry).

Considering the case when  $\lambda > 0$ , for the quadratic piece there are two possibilities:

- $\mu^2 > 0$ : the potential has only the trivial minimum  $\phi = 0$
- $\mu^2 < 0$ : the minimum is every point belong to the circle (in the  $\phi_1, \phi_2$ ) of radius  $\nu$  such that:

$$(\phi_1)^2 + (\phi_2)^2 = \nu^2 \quad \text{with } \nu^2 = -\frac{\mu^2}{\lambda} \quad (1.34)$$

as shown in Figure 1.1

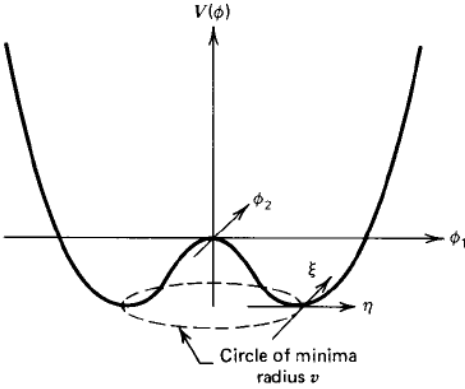


Figure 1.1: The potential  $V(\phi)$  for a complex scalar field with  $\lambda > 0$  and  $\mu^2 < 0$ .

Owing to the U(1) phase-invariance of the Lagrangian 1.33, there is an infinite number of degenerate states of minimum energy. By choosing a particular solution,  $\phi_1 = \nu$  and  $\phi_2 = 0$ , as the ground state, the symmetry gets spontaneously broken. Parametrising the excitations over the ground state as:

$$\phi(x) \equiv \frac{1}{\sqrt{2}}[\nu + \eta(x) + i\xi(x)] \quad (1.35)$$

and substituting into 1.33, one obtains:

$$\mathcal{L}' = \frac{1}{2}(\partial_\mu \xi)^2 + \frac{1}{2}(\partial_\mu \eta)^2 + \mu^2 \eta^2 + \text{const.} + O(\eta^3) + O(\xi^3) \quad (1.36)$$

The third term has the form of a mass term for  $\eta$ -field: the  $\eta$ -mass is  $m_\eta = \sqrt{-2\mu^2}$ . The first term in 1.36 represents the kinetic energy of the  $\xi$ -field but there is no corresponding mass term for the  $\xi$ . The fact there are massless excitations associated with the SSB mechanism is completely general result, known as the *Goldstone theorem*: if a Lagrangian is invariant under a continuous symmetry group  $G$ , but the vacuum is only invariant under a subgroup  $H \subset G$ , then there must exist as many massless spin-0 particles (Goldstone bosons) as broken generators (i.e., generators of  $G$  which do not belong to  $H$ ).

### The Higgs Mechanism

Let's move to consider the case for spontaneous breaking of U(1) local gauge symmetry. Taking into account the covariant derivative 1.8 where the gauge field transforms as in 1.11, the new Lagrangian can be written as

$$\mathcal{L} = D^\mu \phi^* D_\mu \phi - \mu^2 \phi^* \phi - \lambda (\phi^* \phi)^2 - \frac{1}{4} F_{\mu\nu} F^{\mu\nu} \quad (1.37)$$

If  $\mu^2 > 0$ , 1.37 is just the QED Lagrangian for a charged scalar particle of mass  $\mu$ . For the case  $\mu^2 < 0$ , it is interesting to note that to lowest order in  $\xi$ , 1.35 can be expressed as

$$\phi(x) \equiv \frac{1}{\sqrt{2}} [\nu + \eta(x)] e^{i\xi(x)/\nu} \quad (1.38)$$

and this suggests to use different set of real field:  $h$ ,  $\theta$ ,  $A_\mu$  where now

$$\begin{aligned} \phi(x) &\rightarrow \frac{1}{\sqrt{2}} [\nu + h(x)] e^{i\theta(x)/\nu}, \\ A_\mu &\rightarrow A_\mu + \frac{1}{e\nu} \partial_\mu \theta \end{aligned} \quad (1.39)$$

This is a particular choice of gauge, with  $\theta(x)$  chosen so that  $h$  is real. Substituting 1.39 in 1.37, one obtains:

$$\begin{aligned} \mathcal{L}' = &\frac{1}{2} (\partial_\mu h)^2 - \lambda \nu^2 h^2 + \frac{1}{2} e^2 \nu^2 A_\mu^2 - \lambda \nu h^3 - \frac{1}{4} \lambda h^4 \\ &+ \frac{1}{2} e^2 A_\mu^2 h^2 + \nu e^2 A_\mu^2 h - \frac{1}{4} F_{\mu\nu} F^{\mu\nu} \end{aligned} \quad (1.40)$$

The Goldstone boson does not appear in the theory. That is because it corresponds only to the freedom to make a gauge transformation. The Lagrangian 1.40 describes just two interacting massive particles, a vector gauge boson  $A_\mu$  and a massive scalar  $h$ , which is called a *Higgs particle*. This is called the "*Higgs mechanism*".

Consider now the case of  $SU(2)_L \otimes U(1)_Y$  symmetry [8] with the Lagrangian

$$\mathcal{L} = (D_\mu \phi)^\dagger (D^\mu \phi) - \mu^2 \phi^\dagger \phi - \lambda (\phi^\dagger \phi)^2 \quad (1.41)$$

$D_\mu$  is the covariant derivative 1.23 and  $\phi$  is an  $SU(2)$  doublet of complex scalar fields:

$$\phi(x) \equiv \begin{pmatrix} \phi^+(x) \\ \phi^0(x) \end{pmatrix} \quad (1.42)$$

1.41 is invariant under local  $SU(2)_L \otimes U(1)_Y$  transformations.

In  $\mu^2 < 0$  and  $\lambda^2 > 0$  conditions, to generate gauge boson masses, a vacuum expectation value of  $\phi(x)$  must be chosen:

$$\phi_0 \equiv \frac{1}{\sqrt{2}} \begin{pmatrix} 0 \\ \nu \end{pmatrix} \quad (1.43)$$

In this way, the symmetry is broken and this generates a mass for the corresponding gauge boson. This particular choice of  $\phi_0$  breaks both  $SU(2)$  and  $U(1)_Y$  gauge symmetries but since it is neutral, the  $U(1)_{em}$  remains unbroken and this means the photon remains massless.

Now, substituting the vacuum expectation value  $\phi_0$  for  $\phi(x)$  in the Lagrangian 1.41, the expression for W and Z bosons mass are:

$$M_W^2 = \frac{\nu^2 g^2}{4}, \quad M_Z^2 = \frac{\nu^2 g^2}{4 \cos^2 \theta_W} = \frac{M_W^2}{\cos^2 \theta_W} \quad (1.44)$$

From experimental observation [1]:

$$M_Z = 91.1876 \pm 0.0021 \text{ GeV}, \quad M_W = 80.385 \pm 0.015 \text{ GeV} \quad (1.45)$$

From these experimental numbers, one obtains the electroweak mixing angle:

$$\sin^2 \theta_W = 1 - \frac{M_W^2}{M_Z^2} = 0.22336 \pm 0.00010 \quad (1.46)$$

The scalar vacuum expectation value is:

$$\nu = (\sqrt{2}G_F)^{-1/2} = 246 \text{ GeV} \quad (1.47)$$

where  $G_F = 1.1663787 \times 10^{-5} \text{ GeV}^{-1}$  is the Fermi coupling whose value can be measured with the muon lifetime [9].

From 1.41, the potential  $V(\phi)$  can be seen as:

$$V(\phi) = -\frac{1}{4}\lambda\nu^2 + V_H + V_{HG^2} \quad (1.48)$$

The first term stands for mass of the new Higgs boson:  $m_H = \sqrt{2\lambda\nu^2}$ ; the second represents Higgs boson self-interaction and the last the coupling with the weak bosons (W and Z).

It is interesting to note the same Higgs doublet which generates weak bosons masses can give masses also to leptons and quarks. In particular, let's consider the following Lagrangian:

$$\mathcal{L} = -G_e[(\bar{\nu}_e, \bar{e})_L \begin{pmatrix} \phi^+ \\ \phi^0 \end{pmatrix} e_R + \bar{e}_R (\phi^-, \bar{\phi}^0) \begin{pmatrix} \nu_e \\ e \end{pmatrix}] \quad (1.49)$$

Substituting the expression of  $\phi$ :

$$\phi = \frac{1}{\sqrt{2}} \begin{pmatrix} 0 \\ \nu + h(x) \end{pmatrix} \quad (1.50)$$

into 1.49, the Lagrangian becomes:

$$\mathcal{L} = -\frac{G_e}{\sqrt{2}}\nu(\bar{e}_L e_R + \bar{e}_R e_L) - \frac{G_e}{\sqrt{2}}h(\bar{e}_L e_R + \bar{e}_R e_L) \quad (1.51)$$

Choosing  $G_e$  so that  $m_e = G_e \nu / \sqrt{2}$ , since the  $G_e$  is arbitrary, the actual mass of the electron is not predicted.

The quark masses are generated in the same way with the difference that to generate a mass for the upper member of a quark doublet, a new Higgs doublet from  $\phi$  must be used:

$$\phi_c = i\tau\phi^* = \begin{pmatrix} -\bar{\phi}^0 \\ \phi^- \end{pmatrix} \xrightarrow{\text{breaking}} \frac{1}{\sqrt{2}} \begin{pmatrix} \nu + h(x) \\ 0 \end{pmatrix} \quad (1.52)$$

The new Lagrangian can be written as:

$$\mathcal{L} = -G_d(\bar{u}, \bar{d})_L \begin{pmatrix} \phi^+ \\ \phi^0 \end{pmatrix} d_R - G_u(\bar{u}, \bar{d})_L \begin{pmatrix} -\bar{\phi}^0 \\ \phi^- \end{pmatrix} u_R + \text{hermitian conjugate} \quad (1.53)$$

In 1.53, the (u, d) quark doublet are considered even if the weak interactions operate on  $(u, d')_L$  where the primed states are linear combinations of the flavour eigenstates<sup>4</sup>. Using these new doublets, 1.53 is therefore of the form:

$$\mathcal{L} = -G_d^{ij}(\bar{u}, \bar{d})_L \begin{pmatrix} \phi^+ \\ \phi^0 \end{pmatrix} d_{jR} - G_u^{ij}(\bar{u}, \bar{d})_L \begin{pmatrix} -\bar{\phi}^0 \\ \phi^- \end{pmatrix} u_{jR} + \text{hermitian conjugate} \quad (1.54)$$

with  $i, j = 1, \dots, N$ , where  $N$  is the number of quark doublet. Substituting  $\phi_c$  expression, the masses depend on the arbitrary couplings  $G_{u,d}$  but, as for electron, it cannot be predicted.

The choose of a particular single Higgs doublet is sufficient on one hand to generate the masses of both the gauge bosons and the fermions but on the other hand, the masses of the fermions are just parameteres of the theory and are not predicted.

To summarise, the complete Lagrangian of the SM is:

$$\begin{aligned} \mathcal{L}_{SM} = & \frac{1}{4} W_{\mu\nu} \cdot W^{\mu\nu} - \frac{1}{4} B_{\mu\nu} B^{\mu\nu} + \bar{L} \gamma^\mu (i\partial_\mu - g \frac{1}{2} \tau \cdot W_\mu - g' \frac{Y}{2} B_\mu) L \\ & + \bar{R} \gamma^\mu (i\partial_\mu - g' \frac{Y}{2} B_\mu) R + |i\partial_\mu - g \frac{1}{2} \tau \cdot W_\mu - g' \frac{Y}{2} B_\mu|^2 - V\phi \\ & - (G_1 \bar{L} \phi R + G_2 \bar{L} \phi_c R + \text{hermitian conjugate}) \end{aligned} \quad (1.55)$$

The first two terms represent the  $W^\pm$ , Z,  $\gamma$  kinetic energies and the self-interactions; the third and the fourth term the lepton and quark kinetic energies and their interaction with weak W, Z and  $\gamma$ ; the last terms stand for masses and coupling of the Higgs, bosons, leptons and quark.

Without the Higgs boson, the calculability of the SM would have been spoiled. In particular, perturbative unitarity [10, 11] would be lost at high energies as the longitudinal W/Z boson scattering amplitude would grow as the centre-of-mass energy increases. Moreover, the radiative corrections to the gauge boson self-energies would exhibit dangerous logarithmic divergences that would be difficult to reconcile with ElectroWeak

---

<sup>4</sup>Linear combination of the flavour eigenstates considering Cabibbo-Kobayashi-Maswaka (CKM) matrix:  $d'_i = \sum_{n=1}^N V_{in} d_n$  where  $N = 3$  is the number of quarks,  $V_{in}$  is CKM matrix and  $d_n$  are the d type quarks d, s, b.

precision data. With the discovery of the Higgs boson, it has been experimentally established that the SM is based on a gauge theory that could a priori be consistently extrapolated to the Planck scale.

## 1.2 The Higgs boson

The SM Higgs boson is a CP-even scalar of spin 0 [1]. Its mass is given by  $m_h = \sqrt{2\lambda\nu^2}$ , where  $\lambda$  is the Higgs self-coupling parameter in the potential  $V(\phi)$ . The experimentally Higgs mass,  $m_h \simeq 125 \text{ GeV}$  [12][13], implies  $\lambda \simeq 0.1$ .

The Higgs boson couplings to the fundamental particles are set by their masses: very weak for light particles, such as up and down quarks, and electrons, but strong for heavy particles such as the W and Z bosons and the top quark. In particular, the SM Higgs coupling to fundamental fermions are linearly proportional to the fermion masses  $m_f$  ( $y_f = m_f/\nu$  where  $y_f$  is the Yukawa coupling) whereas the couplings to bosons are proportional to the squares of the boson masses. As consequence, the dominant mechanism for Higgs boson production and decay involve the coupling of H to W, Z and/or the third generation quarks and leptons. The Higgs boson coupling to gluons is induced at leading order by a one-loop process in which H couples to a virtual  $t\bar{t}$  pair. Likewise, the Higgs boson couplings to photons is also generated via loops, although in this case the one-loop graph with a virtual  $W^+W^-$  pair provides the dominant contribution and the one involving a virtual  $t\bar{t}$  pair is subdominant.

### 1.2.1 The Higgs boson: production mechanisms

The main production mechanisms at the LHC are gluon fusion, weak-boson fusion, associated production with gauge boson and associated production with a pair of top/antitop quarks. The corresponding Feynman diagrams are reported in Figure 1.2; Figure 1.3 summarises the cross section as a function of mass for these dominant Higgs production processes for a center of mass energy of 13 TeV.

#### Production mechanism: gluon fusion

The Higgs boson production mechanism with the largest cross section is the gluon-fusion process:  $gg \rightarrow H + X$ , mediated by the exchange of a virtual, heavy top quark (Figure 1.2a). Contributions from lighter quarks propagating in the loop are suppressed proportional to  $m_q^2$ . QCD radiative corrections to this process are also very important. At the LHC, with a  $\sqrt{s} = 13 \text{ TeV}$ , the value for the production cross section at the next-to next- to next to leading order is [15]:

$$\sigma_{ggF}^{N3LO} = 48.6 \text{ pb}^{+2.2\text{pb}(+4.6\%)}_{-3.3\text{pb}(+6.7\%)} (\text{theory}) \pm 1.6(3.2\%) (\text{PDF} + \alpha_s) \quad (1.56)$$

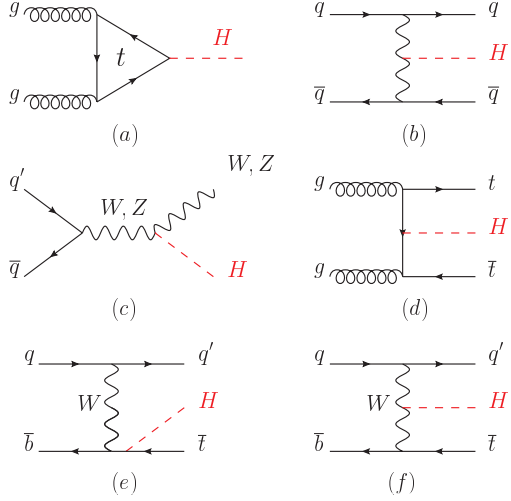


Figure 1.2: Main Leading Order Feynman diagrams contributing to the Higgs production: (a) gluon fusion, (b) Vector-boson fusion, (c) Higgs-strahlung (or associated production with a gauge boson), (d) associated production with a pair of top (or bottom quarks), (e-f) production in association with a single top quark.

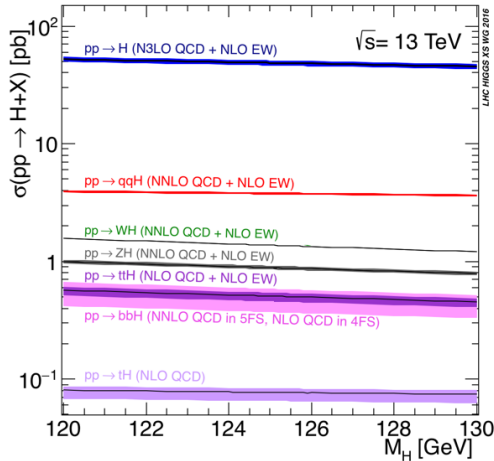


Figure 1.3: Standard Model Higgs boson production cross section at  $\sqrt{s} = 13 \text{ TeV}$  as a function of Higgs boson mass [14].

### Production mechanism: Weak-boson fusion

The SM Higgs production mode with the second-largest cross section is Vector Boson Fusion (VBF):  $q\bar{q} \rightarrow q\bar{q}H$  (Figure 1.2b). This mechanism proceed by the scattering of two (anti-)quarks, mediated by exchange of a W or Z boson, with the Higgs boson radiated off the weak-boson propagator. The scattered quarks give rise to two hard jets in the forward and backward regions of the detector. Gluon radiation in the central-rapidity is suppressed thanks to the color-singlet nature of the weak-gauge boson exchange: this feature let to distinguish VBF from overwhelming QCD backgrounds including gluon-fusion induced Higgs + 2 jets production and production of H in association with a W or Z boson hadronically decaying. This process receive contributions at NLO from QCD and EW; QCD also contributes at NNLO.

### Production mechanism: Higgs-strahlung

The next most relevant Higgs boson production mechanism is the Higgs-strahlung, the production of the Higgs boson with W or Z gauge bosons:  $pp \rightarrow VH+X$  with  $V = W^\pm, Z$  (Figure 1.2c). As in VBF, at NLO EW and QCD (due to corrections to the Drell-Yan cross section) give their contributions to this cross section. In addition, Higgs-strahlung receives non Drell-Yan-like corrections in the  $q\bar{q}$  channels where the Higgs is radiated off top-quarks loops.

### Production mechanism: $t\bar{t}H$

Higgs radiation off top quarks (Figure 1.2d),  $pp \rightarrow t\bar{t}H$ , provides a direct probe of the top-Higgs Yukawa coupling. On the 10th April 2018, CMS announced the observation of the production of the Higgs boson together with a top-quark pair [16].

#### 1.2.2 The Higgs boson: decay channels

As reported in Figure 1.4, the dominant decay modes for the Higgs boson are  $H \rightarrow b\bar{b}$ ,  $H \rightarrow WW^*$  followed by  $H \rightarrow \gamma\gamma$ ,  $H \rightarrow \tau^+\tau^-$  and  $H \rightarrow ZZ^*$ ; Table 1.4 summarises the branching ratios and the relative uncertainty for these decay channels.

## 1.3 Beyond Standard Model (BSM)

Though SM well describes Particle Physics, there are still some questions which it is not equipped to address: e.g. it has no candidate for Dark Matter and it does not include a quantum theory of gravity; it does not have a satisfactory mechanism for generating neutrino masses and does not explain or stabilise the hierarchy of mass scales in physics. In order to try to solve these issues many models have been developed beyond standard model.

The easiest way to extend the SM it with and additional U(1)' group with the associated Z' gauge boson.

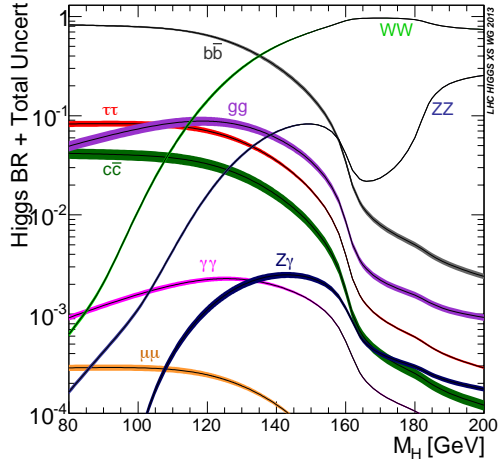


Figure 1.4: Standard Model Higgs boson production cross section at  $\sqrt{s} = 13 \text{ TeV}$  as a function of Higgs boson mass [14].

Decay channel	Branching ratio	Rel. uncertainty
$H \rightarrow b\bar{b}$	$5.84 \times 10^{-1}$	+3.2% -3.3%
$H \rightarrow WW^*$	$2.14 \times 10^{-1}$	+4.3% -4.2%
$H \rightarrow \tau^+\tau^-$	$6.27 \times 10^{-2}$	+5.7% -5.7%
$H \rightarrow ZZ^*$	$2.62 \times 10^{-2}$	+4.3% -4.1%
$H \rightarrow \gamma\gamma$	$2.27 \times 10^{-3}$	+5.0% -4.9%
$H \rightarrow \mu\mu$	$2.18 \times 10^{-4}$	+6.0% -5.9%

Table 1.4: Standard Model leptons features [17] [18].



## Chapter 2

# The CMS detector at LHC

### 2.1 The Large Hadron Collider

Approved in the early '90s and started up in the 2008, the *Large Hadron Collider* (LHC) is currently the world's largest and most powerful particle accelerator. Its main purpose is to help in testing the predictions of different theories of particle physics.

LHC [19], situated at the CERN laboratories of Geneva, is a proton-proton ( $pp$ ) collider built to work at the design center of mass energy of  $\sqrt{s} = 14$  TeV, with a bunch crossing every 25 ns and a design luminosity of  $10^{34} \text{ cm}^{-2}\text{s}^{-1}$ . It is installed in the same circular underground tunnel occupied until the year 2000 by the Large Electron Positron collider (LEP). The  $pp$  collision are used, instead of the  $e^+e^-$  one of LEP, to reduce the synchrotron radiation, in order to accelerate the particles up to a very large energy. It was preferred to a  $p\bar{p}$  collider because it allows to reach higher rate of events. In fact the low anti-proton production efficiency ( $10^5$  protons are needed to create an anti-proton) and larger time needed to accumulate them, would make almost impossible to reach the high design luminosity of the LHC. The luminosity  $L$  is the parameter to quantify the performances of a collider, because the event rate  $R_i$  of a given process  $i$ , defined as the number of events occurring per unit of time, can be written as:

$$R_i = \frac{dN_i}{dt} = L \cdot \sigma_i \quad (2.1)$$

where  $\sigma_i$  is the cross section of the process  $i$ . The luminosity depends only on the machine parameters. Assuming a small crossing angle between the beams and Gaussian-shaped beam bunches, the luminosity  $L$  can be written as:

$$L = \frac{fn_b N^2}{4\pi\sigma^2} \quad (2.2)$$

where  $f$  is the revolution frequency of particle bunches,  $n_b$  is the number of bunches rotating in the accelerator,  $N$  is the number of protons in the two colliding bunches and  $\sigma$  is the RMS of beam profile distributions in the plane orthogonal to the beam direction.

In Figure 2.1 is shown the complete scheme of the accelerator chain of the LHC: the proton beam is created by using an electric field to pull the electrons from hydrogen atoms and start the acceleration. Protons are injected into the PS Booster (PSB) at an energy of 50 MeV from Linac2 (Linear Accelerator 2). The booster comprises four superposed rings: this is because at low energy intensity, the quality of the beams suffers from the repulsive forces between particles. By splitting up the injected beam this effect gets reduced. Once the beam reaches the energy of 1.4 GeV it is extracted and injected into Proton Synchrotron (PS). With a circumference of 628 m, the PS accelerates the beams up to 26 GeV when they are extracted and sent to the Super Proton Synchrotron (SPS). Built in the '70, the SPS has a length of 7 km. The beam is injected at 26 GeV, ramped up to 450 GeV and extracted to the LHC. Once the energy-working point is reached, the beams are made to collide at four locations around the LHC, corresponding to the position of four particles detectors: ALICE (*A Large Ion Collider Experiment*), ATLAS (*A Toroidal LHC Apparatus*), CMS (*Compact Muon Solenoid*) and LHCb (*Large Hadron Collider beauty*). In addition to these, there are other three experiment installed at the LHC: TOTEM (*TOTAL Elastic and diffractive cross section Measurement*) installed close to CMS, MoEDAL (*Monopole and Exotics Detector at the LHC*) close to LHCb and LHCf (*Large Hadron Collider forward*) near ATLAS.

The beams at LHC have a bunch structure as a direct consequence of the radio frequency

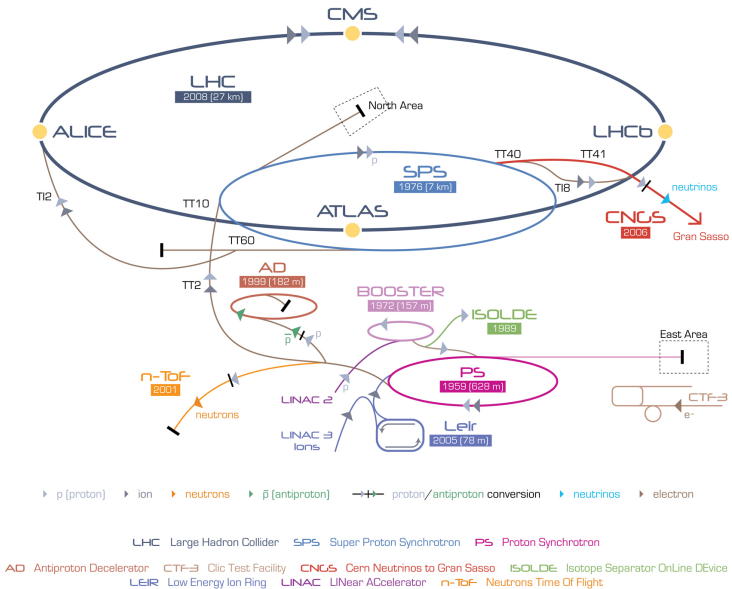


Figure 2.1: Accelerator scheme at CERN.

acceleration scheme. Protons can only be accelerated when the RF field has the correct orientation when particles pass through an accelerating cavity. Under nominal operating conditions, each proton beam has 2808 bunches, with each bunch containing about  $10^{11}$  protons. The bunch size is not constant around the ring getting squeezed as much as

possible around the interaction points in order to increase the probability of collision. They measure a few centimetres long and a millimetre wide when they are far from a collision point; as the bunches approach the collision points, they are squeezed to about  $20\ \mu\text{m}$ . LHC uses a bunch spacing of 25 ns (or 7.5 m) corresponding to a frequency of 2406 MHz.

In Table 2.1 are reported the designed LHC parameters and the ones reached at the end of RunII in 2018.

		Design	2018
<b>Centre of mass energy</b>	$E$	14 TeV	13 TeV
<b>Luminosity</b>	$L$	$10^{34}\ \text{cm}^{-2}\text{s}^{-1}$	—
<b>Time spacing</b>		25 ns	25 ns
<b>Num. of bunches</b>	$k_B$	2808	—
<b>Num. protons per bunch</b>	$N_p$	$1.15 \times 10^{11}$	—

Table 2.1: LHC parameters

## 2.2 The Compact Muon Solenoid

The Compact Muon Solenoid (CMS) is one of the general purpose experiments which takes data at the LHC. Its physics goals range from the search for the Higgs boson to the searches for physics beyond the Standard Model, to the precision measurements of already known particles and phenomena [20].

The overall layout of CMS is shown in Figure 2.2. The inner tracker and the two calorimeters of CMS are located inside a 13 m-long, 5.9 m inner diameter, 3.8 T superconducting solenoid. In order to achieve good momentum resolution within a compact spectrometer without making stringent demands on muon-chamber resolution and alignment, a high magnetic field was chosen. The return field is large enough to saturate 1.5 m of iron, allowing four muon stations to be integrated to ensure robustness and full geometric coverage. The central part of CMS is called *barrel* while the two edges of the detector are denoted as *endcaps*. The tracking volume is given by a cylinder of length 5.8 m and diameter 2.6 m. In order to deal with high track multiplicities, CMS employs 10 layers of silicon microstrip detectors, which provide the required granularity and precision. In addition, 3 layers of silicon pixel detectors are placed close to the interaction region to improve the measurement of the impact parameter of charged-particle tracks, as well as the position of secondary vertexes. The electromagnetic calorimeter (ECAL) uses lead tungstate ( $\text{PbWO}_4$ ) crystals with coverage in pseudorapidity up to  $|\eta| < 3.0$ . A preshower system is installed in front of the edges of ECAL for  $\pi^0$  rejection.

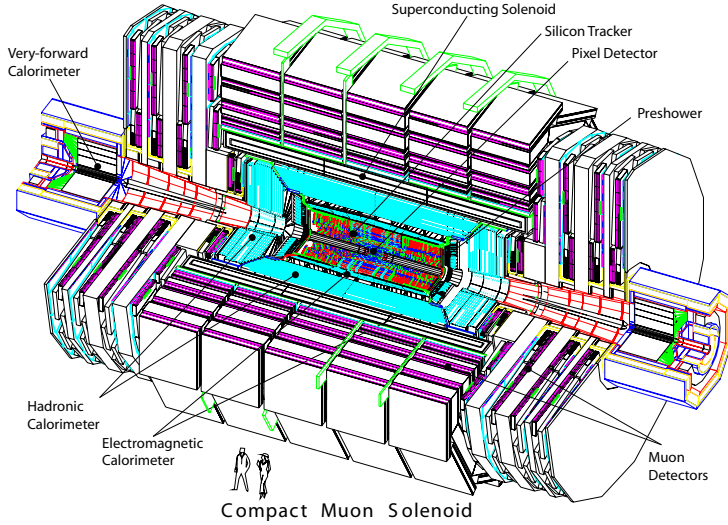


Figure 2.2: CMS detector overview.

### Coordinate Conventions

The coordinate system adopted by CMS has the origin centered at the nominal collision point inside the experiment, the  $y$ -axis pointing vertically upward, and the  $x$ -axis pointing radially inward toward the center of the LHC. Thus, the  $z$ -axis points along the beam direction toward the Jura mountains from LHC Point 5. The azimuthal angle  $\phi$  is measured from the  $x$ -axis in the  $x$ - $y$  plane. The polar angle  $\theta$  is measured from the  $z$ -axis. Pseudorapidity is defined as

$$\eta = -\ln \tan(\theta/2) \quad (2.3)$$

The value  $\eta = 0$  corresponds to a direction perpendicular to the beamline, while the limit  $\eta = \infty$  gives a direction parallel to the beamline. The momentum and energy measured transverse to the beam direction, denoted by  $p_T$  and  $E_T$ , respectively, are computed as follow:

$$p_T = p \sin\theta \quad (2.4)$$

$$E_T = E \sin\theta \quad (2.5)$$

Finally, particles which escape the detection leave an imbalance in the transverse plane which is quantified as missing transverse energy in the following way:

$$E_T^{miss} = - \sum_i p_T^i \quad (2.6)$$

as the negative vectorial sum of the transverse momentum of all the visible particles in the event.

### 2.2.1 The tracking system

The tracker [21, 22], placed within the magnetic field, is the subdetector which is closer to the interaction point. It is dedicated to track and vertex finding. The silicon (Si) technology has been chosen for the whole tracker in order to provide good radiation hardness, high granularity and large hit redundancy to perform a good pattern recognition. The layout of the CMS tracker is shown in Figure 2.3. Close to the interaction vertex, in the barrel region, are 3 layers of hybrid pixel detectors at a radius ( $r$ ) of about 4, 7 and 10 cm. The size of the pixel detector is  $100 - 150 \text{ m}^2$ . In the barrel part, the Si microstrip detectors are placed at  $r$  between 20 and 110 cm. The forward region has 2 pixel and 9 microstrip layers in each of the two endcaps. In order to avoid excessively shallow track crossing angles, the Inner Barrel is shorter than the Outer Barrel, and there are additional three Inner Disks in the transition region between barrel and endcaps, on each side of the Inner Barrel. The total area of the Si detectors is around  $200 \text{ m}^2$ , providing a coverage up to  $\eta = 2.5$ . The material budget inside the active volume of the tracker increases from 0.4 radiation length ( $X_0$ ) at  $\eta = 0$  to around 1  $X_0$  at  $|\eta| = 1.6$ , before decreasing to 0.6  $X_0$  at  $|\eta| = 2.5$ .

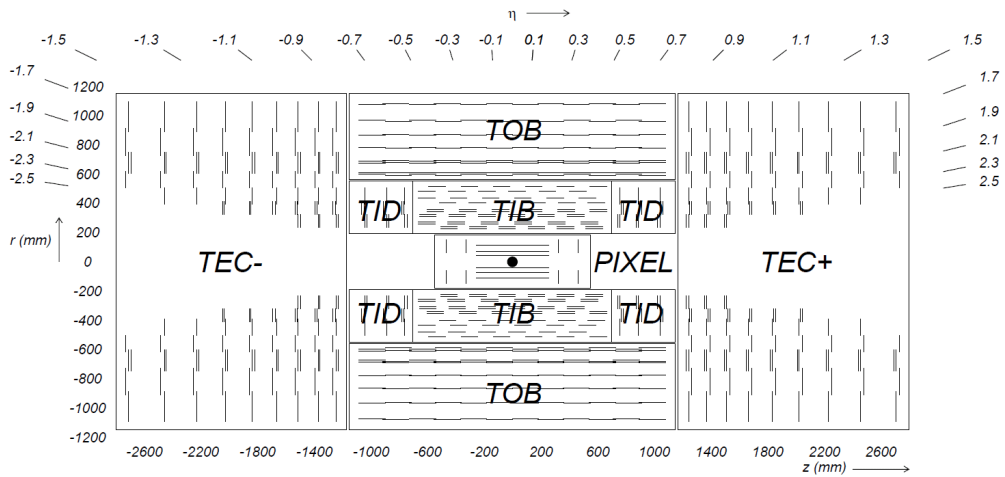


Figure 2.3: Schematic cross section through the CMS tracker in the  $r - z$  plane: each line represents a detector module. Double lines indicate back-to-back modules which deliver stereo hits.

#### The pixel detector

The pixel detector is the part of the tracking system that is closest to the interaction region and covers a pseudorapidity range  $-2.5 < \eta < 2.5$ , matching the acceptance of the central tracker. Figure 2.4 shows the geometric pixel structure. It contributes precise tracking points in  $r - \phi$  and  $z$  and therefore is responsible for a small impact parameter resolution that is important for good secondary vertex reconstruction. With a pixel cell

size of  $100 \times 150 \mu\text{m}^2$  emphasis has been put on achieving similar track resolution in both  $r - \phi$  and z directions:  $10 \mu\text{m}$  in  $r - \phi$  direction and  $20 \mu\text{m}$  along z. The pixel detector is essential for the reconstruction of secondary vertices from b and tau decays, and forming seed tracks for the outer track reconstruction and high level triggering. It consists of three barrel layers (BPix) with two endcap disks (FPix). The 53-cm-long BPix layers will be located at mean radii of 4.4, 7.3 and 10.2 cm. The FPix disks, extending from  $\approx 6$  to 15 cm in radius, will be placed on each side at  $z = \pm 34.5$  and  $z = \pm 46.5$  cm. BPix (FPix) contain 48 million (18 million) pixels covering a total area of  $0.78$  ( $0.28$ )  $\text{m}^2$ . The arrangement of the 3 barrel layers and the forward pixel disks on each side gives 3 tracking points over almost the full  $\eta$  range. In the high  $\eta$  region the 2 disk points are combined with the lowest possible radius point from the 4.4 cm barrel layer.

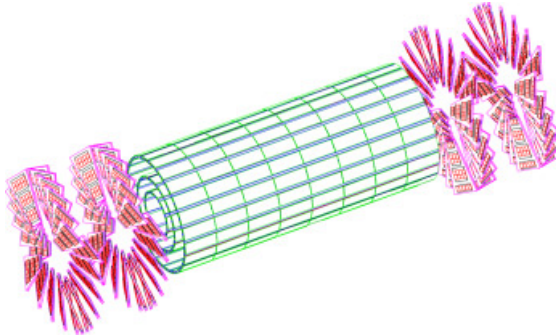


Figure 2.4: Geometrical layout of the pixel detector.

### **Pixel Upgrade**

Due to the radiation damage and significant data losses due to high occupancy in the readout chip of the pixel detector, the pixel system has been replaced by a new one in the end-of-year shutdown during winter 2016/2017 in order to maintain the excellent tracking and other physics performances [23]. The main new features of the upgraded pixel detector are a ultra-light mechanical design with four barrel layers and three end-cap disks, digital readout chip with higher rate capability and a new cooling system. The geometrical layout of the upgrade system, shown in Figure 2.5, consists of four cylindrical barrel layers placed at radii of 29, 68, 109, 160 mm and three disks in each of the forward regions placed at a distance from the nominal interaction point of 291, 396 and 516 mm. This layout is optimized in order to offer full 4-hit tracking coverage up to pseudorapidities of 2.5, with an increased redundancy compared to the present system.

### **The silicon strip detector**

The silicon strip detector is composed of three different subsystem. The Tracker Inner Barrel and Disks (TIB/TID see Figure 2.3) are composed of 4 barrel layers, supplemented by 3 disks at each end. TIB/TID delivers up to 4  $r - \phi$  measurements on a trajectory

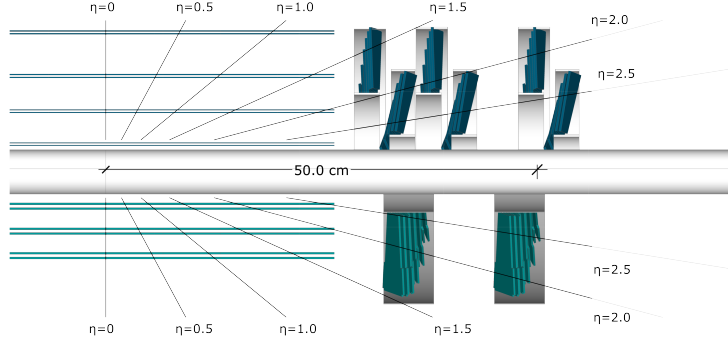


Figure 2.5: Comparison of the geometrical layouts of the old (bottom) and upgraded (top) CMS pixel detectors.

using  $320 \mu\text{m}$  thick silicon microstrip sensors with their strips parallel to the beam axis in the barrel and radial on the disks. The strip pitch is  $80\mu\text{m}$  on layers 1 and 2 and  $120 \mu\text{m}$  on layers 3 and 4 in the TIB, leading to a single point resolution of  $23 \mu\text{m}$  and  $35 \mu\text{m}$ , respectively. In the TID the mean pitch varies between  $100\mu\text{m}$  and  $141\mu\text{m}$ . The TIB/TID is surrounded by the Tracker Outer Barrel (TOB). It has an outer radius of 116 cm and consists of 6 barrel layers of  $500\mu\text{m}$  thick microstrip sensors with strip pitches of  $183\mu\text{m}$  on the first 4 layers and  $122\mu\text{m}$  on layers 5 and 6. It provides another 6  $r - \phi$  measurements with single point resolution of  $53\mu\text{m}$  and  $35\mu\text{m}$ , respectively. The TOB extends in  $z$  between  $\pm 118\text{cm}$ . Beyond this  $z$  range the Tracker EndCaps ( $\pm\text{TEC}$ , where the sign indicates the location along the  $z$  axis) cover the region  $124 \text{ cm} < |z| < 282 \text{ cm}$  and  $22.5 \text{ cm} < |r| < 113.5 \text{ cm}$ . Each TEC is composed of 9 disks, carrying up to 7 rings of silicon microstrip detectors ( $320\mu\text{m}$  thick on the inner 4 rings,  $500\mu\text{m}$  thick on rings 5-7) with radial strips of  $97\mu\text{m}$  to  $184\mu\text{m}$  average pitch. Thus, they provide up to 9  $\phi$  measurements per trajectory. In addition, the modules in the first two layers and rings, respectively, of TIB, TID, and TOB as well as rings 1, 2, and 5 of the TECs carry a second microstrip detector module which is mounted back-to-back with a stereo angle of 100 mrad in order to provide a measurement of the second coordinate ( $z$  in the barrel and  $r$  on the disks). The achieved single point resolution of this measurement is  $230\mu\text{m}$  and  $530\mu\text{m}$  in TIB and TOB, respectively, and varies with pitch in TID and TEC. The sensor elements in the strip tracker are single sided p-on-n type silicon micro-strip sensors shown in Figure 2.6: in TIB/TID and on the inner 4 rings of the TECs, thin sensors of  $(320 \pm 20) \mu\text{m}$  wafer thickness are used, with substrate resistivity of  $\rho = 1.55 - 3.25 \text{ k}\Omega\text{cm}$ ; TOB and the outer 3 rings of the TECs are equipped with thicker sensors of  $(500 \pm 20) \mu\text{m}$  thickness, with substrate resistivity of  $\rho = 4 - 8 \text{ k}\Omega\text{cm}$ .

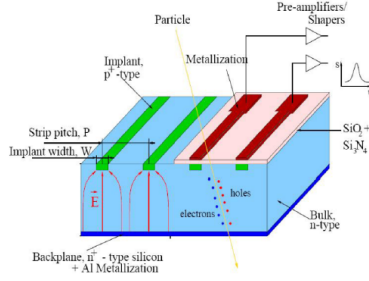


Figure 2.6: Single sided p-on-n type silicon micro-strip sensor.

### 2.2.2 Electromagnetic calorimeter

The electromagnetic calorimeter plays an essential role in the study of the physics of electroweak symmetry breaking, and in the exploration of beyond the Standard Model scenarios. ECAL is a homogeneous calorimeter of almost 76000 Lead Tungstate PbWO<sub>4</sub> scintillating crystals divided into a barrel and two endcaps. A 3D view of the barrel and endcap electromagnetic calorimeter is shown in Figure 2.7.

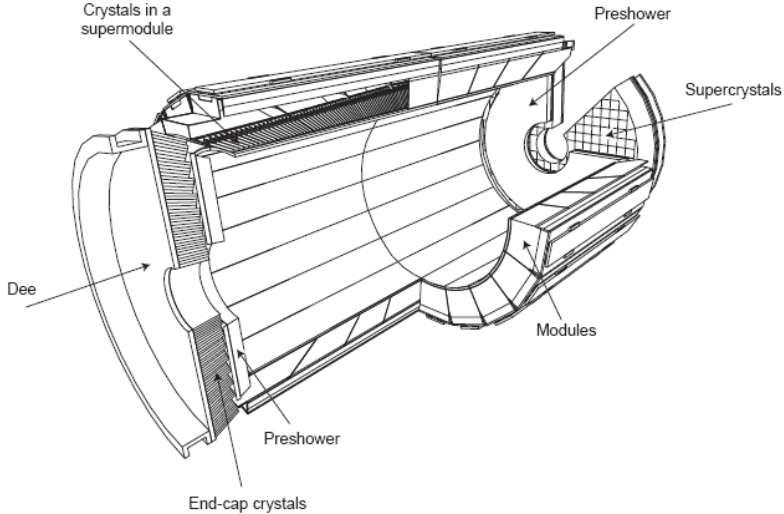


Figure 2.7: A 3D view of the electromagnetic calorimeter.

#### The Barrel Calorimeter

The barrel part of the ECAL covers the pseudorapidity range  $|\eta| < 1.479$ . The front face of the crystals is at a radius of 1.29 m and each crystal has a square cross-section of  $22 \times 22 \text{ mm}^2$  and a length of 230 mm corresponding to  $25.8 X_0$ . The truncated pyramid-shaped crystals are mounted in a geometry which is off-pointing with respect to the mean

position of the primary interaction vertex, with a  $3^\circ$  tilt in both  $\phi$  and in  $\eta$ . The crystal cross-section corresponds to  $\Delta\eta \times \Delta\phi = 0.0175 \times 0.0175$  ( $1^\circ$ ). The barrel granularity is 360-fold in  $\phi$  and  $(2 \times 85)$ -fold in  $\eta$ , resulting in a total number of 61 200 crystals. The crystal volume in the barrel amounts to  $8.14 \text{ m}^3$  (67.4 t). Crystals for each half-barrel are grouped in 18 supermodules each subtending  $20^\circ$  in  $\phi$ . Each supermodule comprises four modules with 500 crystals in the first module and 400 crystals in each of the remaining three modules. For simplicity of construction and assembly, crystals have been grouped in arrays of  $2 \times 5$  crystals which are contained in a very thin wall ( $200 \mu\text{m}$ ) alveolar structure and form a submodule. Thermal regulation is carried out by two active systems: 1) a specially regulated cooling circuit which keeps the operating temperature (ambient temperature) of the crystal array within a tight temperature spread of  $\pm 0.05^\circ\text{C}$ , ensuring adequate thermal stability; 2) the power cooling circuit evacuates the heat generated by all power sources in the supermodule (each supermodule is designed as a separate thermal entity).

### The Endcap Calorimeter

The endcap part of the crystal calorimeter covers a pseudorapidity range from 1.48 to 3.0. The design of the endcaps provides precision energy measurement up to  $|\eta| = 2.5$ . Crystals are however installed up to  $|\eta| = 3$  in order to augment the energy-flow measurement in the forward direction. The mechanical design of the endcap calorimeter is based on an offpointing pseudo-projective geometry using tapered crystals of the same shape and dimensions ( $24.7 \times 24.7 \times 220 \text{ mm}^3$ ) grouped together into units of 36, referred to as supercrystals. A total of 268 identical supercrystals is used to cover each endcap with a further 64 sectioned supercrystals used to complete the inner and outer perimeter. Each endcap contains 7324 crystals, corresponding to a volume of  $1.52 \text{ m}^3$  (12.6 t). Both endcaps are identical. Each endcap detector is constructed using Dee-shaped sections. Because of the high radiation levels in the endcaps all materials used in this region must tolerate very large doses and neutron fluences.

The endcap part also includes the preshower detector.

### The Preshower Detector

The endcap preshower covers a pseudorapidity range from  $|\eta| = 1.65$  to 2.61. Its main function is to provide  $\pi^0$ - $\gamma$  separation. The preshower detector, placed in front of the crystals, contains two lead converters of a total thickness of  $2 X_0$  and  $1 X_0$  respectively, followed by detector planes of silicon strips with a pitch of  $< 2 \text{ mm}$ . The impact position of the electromagnetic shower is determined by the center-of-gravity of the deposited energy. The accuracy is typically  $300 \mu\text{m}$  at 50 GeV. In order to correct for the energy deposited in the lead converter, the energy measured in the silicon is used to apply corrections to the energy measurement in the crystal. The fraction of energy deposited in the preshower (typically 5% at 20 GeV) decreases with increasing incident energy.

### Energy Resolution

For the energy range of about 25 GeV to 500 GeV, the ECAL energy resolution has been parameterized as:

$$\frac{\sigma(E)}{E} = \frac{a}{\sqrt{E}} \oplus \frac{\sigma_n}{E} \oplus c \quad (\text{E in GeV}) \quad (2.7)$$

where  $a$  is the stochastic term,  $\sigma_n$  the noise, and  $c$  the constant term. Figure 2.8 summarizes the different contributions expected for the energy resolution. Terms representing the degradation of the energy resolution at extremely high energies have not been included. The stochastic term includes fluctuations in the shower containment as well as a contribution from photostatistics. The noise term contains the contributions from electronic noise and pile-up energy; the former is quite important at low energy, the latter is negligible at low luminosity. The curve labeled *intrinsic* includes the shower containment and a constant term of 0.55%. The constant term must be kept down to this level in order to profit from the excellent stochastic term of PbWO<sub>4</sub> in the energy range relevant for the search for new physics. To achieve this goal, in situ calibration/monitoring using isolated high  $p_T$  electrons is performed.

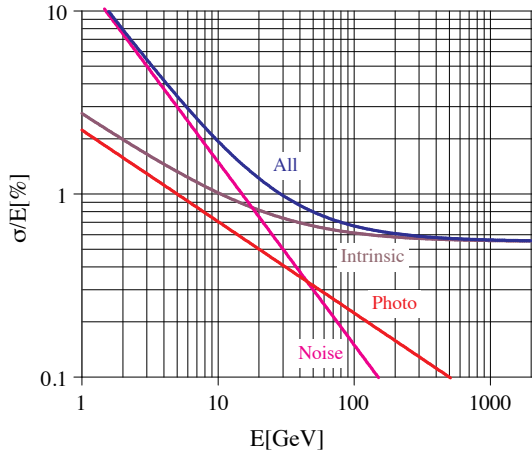


Figure 2.8: Different contributions to the energy resolution of the PbWO<sub>4</sub> calorimeter.

### 2.2.3 Hadronic Calorimeter

Figure 2.9 shows the longitudinal view of the CMS detector with the locations od the hadron calorimeters [25]. The dashed lines are at fixed  $\eta$  values. The hadron calorimeter barrel and endcaps sit behind the tracker and the electromagnetic calorimeter as seen from the interaction point. The hadron calorimeter barrel is radially restricted between the outer extent of the electromagnetic calorimeter ( $R = 1.77$  m) and the inner extent of the magnet coil ( $R = 2.95$  m). This constrains the total amount of material which can be put in to absorb the hadronic shower. Therefore, an outer hadron calorimeter or tail

catcher is placed outside the solenoid complementing the barrel calorimeter. Beyond  $|\eta| = 3$ , the forward hadron calorimeters placed at 11.2 m from the interaction point extend the pseudorapidity coverage down to  $|\eta| = 5.2$  using a Cherenkov-based, radiation-hard technology.

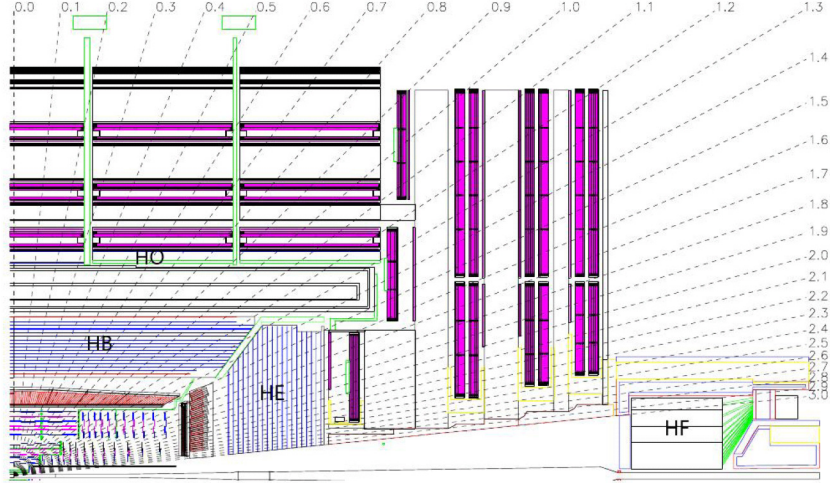


Figure 2.9: Longitudinal view of the CMS detector showing the locations of the hadron barrel (HB), endcap (HE), outer (HO) and forward (HF) calorimeters.

### Hadron barrel (HB)

The HB is a sampling calorimeter covering the pseudorapidity range  $|\eta| < 1.3$ . It is divided into two half-barrel sections, each half-section being inserted from either end of the barrel cryostat of the superconducting solenoid and subsequently hung from rails in the median plane. The HB consists of 36 identical azimuthal wedges which form the two half-barrels (HB+ and HB-). The wedges are constructed out of flat brass absorber plates aligned parallel to the beam axis. Each wedge is segmented into four azimuthal angle ( $\phi$ ) sectors. The plates are bolted together in a staggered geometry resulting in a configuration that contains no projective dead material for the full radial extent of a wedge. The innermost and outermost plates are made of stainless steel for structural strength. The plastic scintillator is divided into 16  $\eta$  sectors, resulting in a segmentation  $(\Delta\eta, \Delta\phi) = (0.087, 0.087)$ . The wedges are themselves bolted together, in such a fashion as to minimize the crack between the wedges to less than 2 mm. The absorber consists of a 40-mm-thick front steel plate, followed by eight 50.5- mm-thick brass plates, six 56.5-mm-thick brass plates, and a 75-mm-thick steel back plate. The total absorber thickness at  $90^\circ$  is 5.82 interaction lengths ( $\lambda_I$ ). The HB effective thickness increases with polar angle ( $\theta$ ) as  $1/\sin\theta$ , resulting in 10.6  $\lambda_I$  at  $|\eta| = 1.3$ . The electromagnetic crystal calorimeter in front of HB adds about 1.1  $\lambda_I$  of material.

### **Hadron endcap (HE)**

The hadron calorimeter endcaps (HE) cover a substantial portion of the rapidity range,  $1.3 < |\eta| < 3$ . Since the calorimeter is inserted into the ends of a 4-T solenoidal magnet, the absorber must be made from a non-magnetic material in order not to distort it. It must also have a maximum number of interaction lengths to contain hadronic showers, good mechanical properties and reasonable cost, leading to the choice of C26000 cartridge brass. The endcaps are attached to the muon endcap yoke. Only a small part of the calorimeter structure can be used for the fixation to the magnet iron, because the majority of the space between HE and muon absorber is occupied with muon cathode strip chambers. A 10-t electromagnetic calorimeter (EE) with a 2-t preshower detector (ES) is attached at the front face of HE. The design of the absorber is driven by the need to minimize the cracks between HB and HE, rather than single-particle energy resolution, since the resolution of jets in HE will be limited by pileup, magnetic field effects, and parton fragmentation. The plates are bolted together in a staggered geometry resulting in a configuration that contains no projective dead material. The design provides a self-supporting hermetic construction. The brass plates are 79-mm-thick with 9-mm gaps to accommodate the scintillators. The total length of the calorimeter, including electromagnetic crystals, is about  $10 \lambda_I$ . The granularity of the calorimeters is  $\Delta\eta \times \Delta\phi = 0.087 \times 0.087$  for  $|\eta| < 1.6$  and  $\Delta\eta \times \Delta\phi \approx 0.17 \times 0.17$  for  $|\eta| \geq 1.6$ .

### **Hadron outer (HO)**

In the central pseudorapidity region, the combined stopping power of EB plus HB does not provide sufficient containment for hadron showers. To ensure adequate sampling depth for  $|\eta| < 1.3$ , the hadron calorimeter is extended outside the solenoid with a tail catcher called the HO or outer calorimeter. The HO utilises the solenoid coil as an additional absorber equal to  $1.4/\sin\theta$  interaction lengths and is used to identify late starting showers and to measure the shower energy deposited after HB. Outside the vacuum tank of the solenoid, the magnetic field is returned through an iron yoke designed in the form of five 2.536 m wide (along z-axis) rings. The HO is placed as the first sensitive layer in each of these five rings; the nominal central z positions of the five rings are respectively  $?5.342$  m,  $?2.686$  m, 0,  $+2.686$  m and  $+5.342$  m. At  $\eta = 0$ , HB has the minimal absorber depth. Therefore, the central ring (ring 0) has two layers of HO scintillators on either side of a 19.5 cm thick piece of iron (the tail catcher iron) at radial distances of 3.82 m and 4.07 m, respectively. All other rings have a single HO layer at a radial distance of 4.07 m. The total depth of the calorimeter system is thus extended to a minimum of  $11.8 \lambda_I$  except at the barrel-endcap boundary region. The HO is constrained by the geometry of the muon system. The segmentation of these detectors closely follows that of the barrel muon system. Each ring has 12 identical  $\phi$ -sectors. The 12 sectors are separated by 75-mm-thick stainless steel beams which hold successive layers of iron of the return yoke as well as the muon system.

### Hadron foward (HF)

The forward calorimeter is a cylindrical steel structure with an outer radius of 130.0 cm. The front face of the calorimeter is located at 11.2 m from the interaction point. The hole for the beam pipe is cylindrical, with radius 12.5 cm from the center of the beam line. This structure is azimuthally subdivided into  $20^\circ$  modular wedges. Thirty-six such wedges (18 on either side of the interaction point) make up the HF calorimeters. The fibres run parallel to the beam line, and are bundled to form  $0.175 \times 0.175$  ( $\Delta\eta \times \Delta\phi$ ) towers. The detector is housed in a hermetic radiation shielding which consists of layers of 40 cm thick steel, 40 cm of concrete, and 5 cm of polyethylene. A large plug structure in the back of the detector provides additional shielding. It consists of a steel absorber structure that is composed of 5 mm thick grooved plates. Fibres are inserted in these grooves. The detector is functionally subdivided into two longitudinal segments. Half of the fibres run over the full depth of the absorber (165 cm  $\approx 10 \lambda_I$ ) while the other half starts at a depth of 22 cm from the front of the detector. These two sets of fibres are read out separately. This arrangement makes it possible to distinguish showers generated by electrons and photons, which deposit a large fraction of their energy in the first 22 cm, from those generated by hadrons, which produce nearly equal signals in both calorimeter segments on average. The long fibre section is referred as L (measuring the total signal), and the short fibre section as S (measuring the energy deposition after 22 cm of steel). The absorber has grooves which make a square grid separated by  $5.0 \pm 0.1$  mm center-to-center. Long and short fibres alternate in these grooves. The packing fraction by volume (fibre/total) in the first 22 cm is 0.57% and is twice as large beyond that depth.

## 2.3 Magnet

The required performance of the muon system, and hence the bending power, is defined by the narrow states decaying into muons and by the unambiguous determination of the sign for muons with a momentum of 1 TeV/c. This requires a momentum resolution of  $\Delta p/p \sim 10\%$  at  $p = 1$  TeV. To achieve this goal, CMS chose a large superconducting solenoid, the parameters of which are given in table 2.2.

Parameter	Value
Field	3.8 T
Inner bore	5.9 m
Length	12.9 m
Number of turns	2168
Current	19.5 kA
Stored energy	2.7 GJ

Table 2.2: Parameters of the CMS superconducting solenoid.

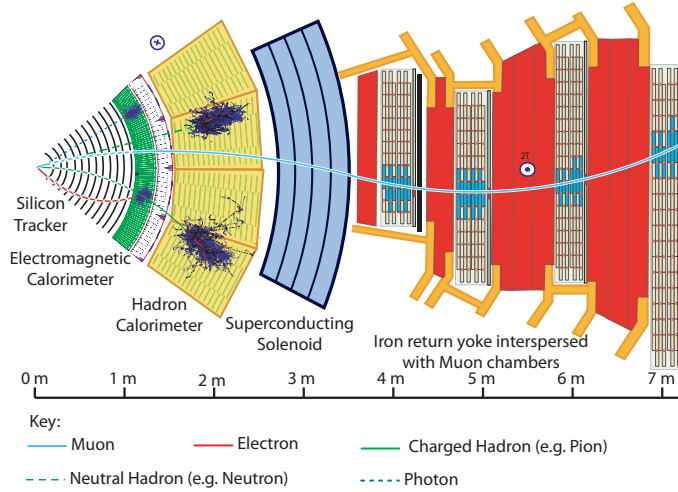


Figure 2.10: Schematic view of a transverse slice of the central part of the CMS detector.

## 2.4 Muon System

The muon system is the outermost of the CMS subdetectors. Its main goals are the identification of muons, thanks to their high penetrating power, and a precise measurement of their momentum, with the help of the information coming from the tracker. The muon system also works as trigger for events which involve muons and it provides a precise time measurement of the bunch crossing. The CMS muon system [26] relies on three kinds of gaseous detectors: drift tubes (DT), cathode strip chambers (CSC) and resistive plate chambers (RPC). The DT and the CSC provide an excellent spatial resolution for the measurement of charged particle momentum; the RPC are used for trigger issues because of the very good timing. The active parts of the muon system are hosted into stations which are interleaved by the iron layers of the return yoke of the magnet. The longitudinal view of a quarter of the muon system is given in Figure 2.11. The barrel extends up to  $|\eta| < 1.4$ , the endcaps up to  $|\eta| < 2.4$ .

### DT

The CMS barrel muon detector consists of 4 stations forming concentric cylinders around the beam line: the 3 inner cylinders have 60 drift chambers each and the outer cylinder has 70. It is possible to use drift chambers as the tracking detectors for the barrel muon system because of the low expected rate and the relatively low strength of the local magnetic field. In each of the 12 sectors of the yoke there are 4 muon chambers per wheel, labeled MB1, MB2, MB3, and MB4, Figure 2.12. The yoke-iron supports that are between the chambers of a station generate 12 unavoidable dead zones in the  $\phi$  coverage, although the supports are placed so as not to overlap in  $\phi$ . A DT chamber is made of 3 (or 2) superlayers (SL, see Figure 2.13), each made of 4 layers of rectangular drift cells

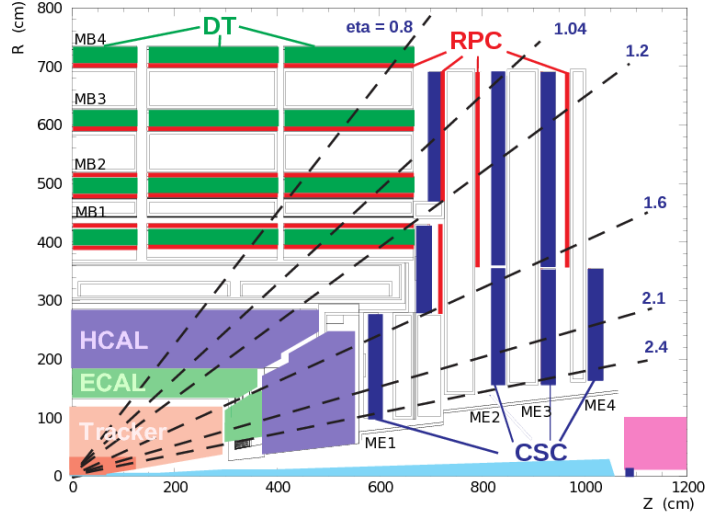


Figure 2.11: Longitudinal view of one quarter of the CMS muon system

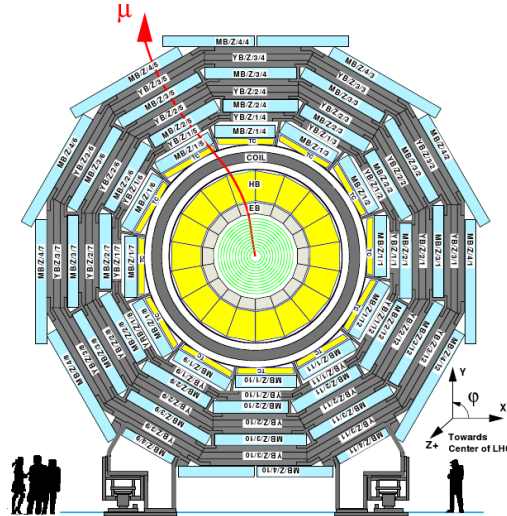


Figure 2.12: Layout of the CMS barrel muon DT chambers in one of the 5 wheels. The chambers in each wheel are identical with the exception of wheels -1 and +1 where the presence of cryogenic chimneys for the magnet shortens the chambers in 2 sectors. Note that in sectors 4 (top) and 10 (bottom) the MB4 chambers are cut in half to simplify the mechanical assembly and the global chamber layout.

staggered by half a cell. The SL is the smallest independent unit of the design. The wires in the 2 outer SLs are parallel to the beam line and provide a track measurement in the magnetic bending plane ( $r\phi$ ). In the inner SL, the wires are orthogonal to the beam line and measure the  $z$  position along the beam. This third,  $z$ -measuring, SL is not present in the fourth station, which therefore measures only the  $\phi$  coordinate. The

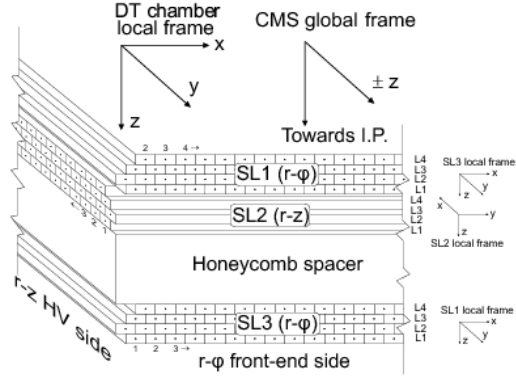


Figure 2.13: Layout of the DT chamber: each chamber is made of 3 Superlayers of Drift Tube and each SL is made of 4 layers of Drift Tube.

main element the in the DT is the drift cell, shown in Figure 2.14: its pitch is 42 mm, while the layer pitch is 13 mm. The gas used is Ar – CO<sub>2</sub> mixture (85% - 15%).

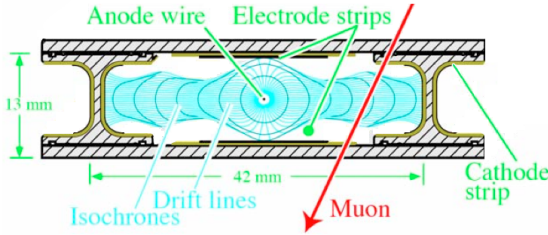


Figure 2.14: Sketch of a cell showing drift lines and isochrones. The plates at the top and bottom of the cell are at ground potential. The voltages applied to the electrodes are +3600V for wires, +1800V for strips, and -1200V for cathodes.

## CSC

CMS Endcap Muon system consists of Cathode Strip Chambers (CSC) arranged in 4 stations (ME1, ME2, ME3, ME4) (Figure 2.15). The chambers are trapezoidal and cover either 10° or 20° in  $\phi$ ; all chambers, except for the ME1/3 ring, overlap and provide contiguous  $\phi$ -coverage. A muon in the pseudorapidity range  $1.2 < |\eta| < 2.4$  crosses 3 or 4 CSCs. In the endcap-barrel overlap range,  $0.9 < |\eta| < 1.2$ , muons are detected by both the barrel drift tubes (DT) and endcap CSCs. The CSCs are multiwire proportional chambers comprised of 6 anode wire planes interleaved among 7 cathode panels (Figure ??). Wires run azimuthally and define a track's radial coordinate. Strips are milled on cathode panels and run lengthwise at constant  $\Delta\phi$  width. The largest chambers, ME2/2 and ME3/2, are about  $3.4 \times 1.5 \text{ m}^2$  in size. The overall area covered by the sensitive planes of all chambers is about  $5000 \text{ m}^2$ , the gas volume is  $\sim 50 \text{ m}^3$ , and the

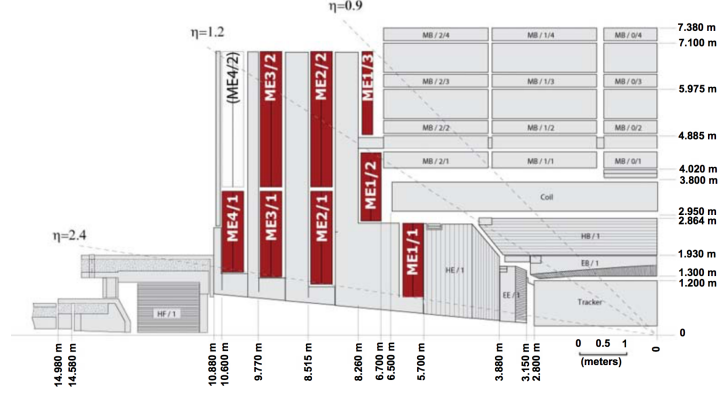


Figure 2.15: Quarter-view of the CMS detector. Cathode strip chambers of the Endcap Muon system are highlighted.

number of wires is about 2 million. There are about 9000 high-voltage channels in the system, about 220 000 cathode strip read-out channels with 12-bit signal digitisation, and about 180 000 anode wire read-out channels. The CSCs provide the functions of precision muon measurement and muon trigger in one device. The nominal gas mixture used is 40%Ar + 50%CO<sub>2</sub> + 10%CF<sub>4</sub>.

## RPC

Resistive Plate Chambers (RPC) are gaseous parallel-plate detectors that combine adequate spatial resolution with a time resolution comparable to that of scintillators. An RPC is capable of tagging the time of an ionising event in a much shorter time than the 25 ns between 2 consecutive LHC bunch crossings (BX). The CMS RPC basic double-gap module consists of 2 gaps, hereafter referred as up and down gaps, operated in avalanche mode with common pick-up read-out strips in between. The total induced signal is the sum of the 2 single-gap signals. Six layers of RPC chambers are embedded in the barrel iron yoke, 2 located in each of the first and second muon stations and 1 in each of the 2 last stations. The redundancy in the first 2 stations allows the trigger algorithm to perform the reconstruction always on the basis of 4 layers, even for low  $p_T$  particles, which may stop inside the iron yoke. In the endcap region, 3 layers up to  $\eta = 1.6$  are built. In the barrel iron yoke, the RPC chambers form 6 coaxial sensitive cylinders (all around the beam axis) that are approximated with concentric dodecagon arrays arranged into 4 stations (Figure 2.17). In the first and second muon stations there are 2 arrays of RPC chambers located internally and externally with respect to the Drift Tube (DT) chambers: RB1in and RB2in at smaller radius and RB1out and RB2out at larger radius. In the third and fourth stations there are again 2 RPC chambers, both located on the inner side of the DT layer (named RB3+ and RB3-, RB4+ and RB4-). A special case is RB4 in sector 4, which consists of 4 chambers: RB4++, RB4+, RB4-, and RB4-. Finally, in sectors 9 and 11 there is only 1 RB4 chamber. In the forward and

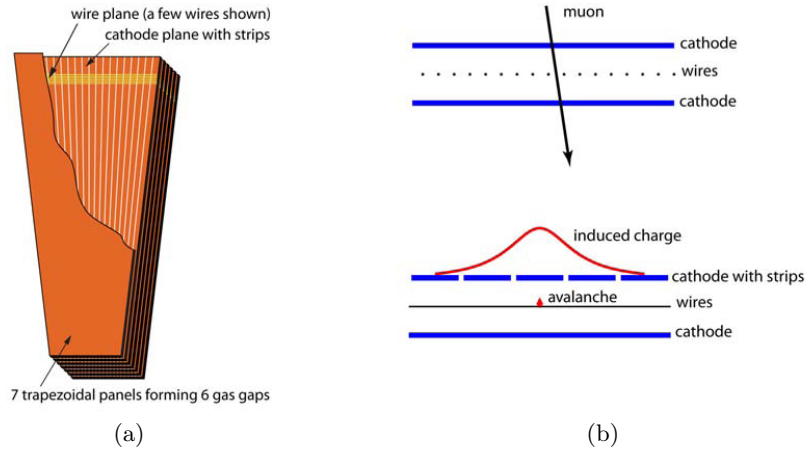


Figure 2.16: (a) Layout of a CSC made of 7 trapezoidal panels. The panels form 6 gas gaps with planes of sensitive anode wires. (b) A schematic view of a single gap illustrating the principle of CSC operation. By interpolating charges induced on cathode strips by avalanche positive ions near a wire, one can obtain a precise localisation of an avalanche along the wire direction.

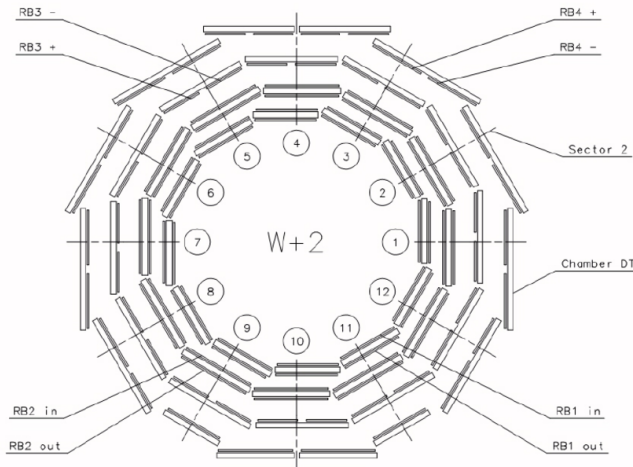


Figure 2.17: Schematic layout of one of the 5 barrel wheels, which are labeled ?2, ?1, 0, +1, and +2, respectively. Each wheel is divided into 12 sectors that are numbered as shown.

backward regions of the CMS detector, 3 iron disks constitute the endcap yokes.

## GEM

After the upgrade of the LHC injector chain during the second Long Shutdown (LS2), which is currently planned to take place around 2019, the instantaneous luminosity ( $\mathcal{L}$ ) will approach or exceed  $2 \times 10^{34} \text{ cm}^{-2} \text{ s}^{-1}$ . In order to maintain the high level of performance achieved during Run 1 and Run 2 in the challenging environment of the high luminosity LHC collider (HL-LHC), muon system will improved installing an additional set of muon detectors, GE1/1 (see Figure 2.18), that use gas electron multiplier (GEM) technology in the first endcap muon station in order to maintain or even improve the forward muon triggering and reconstruction in the region  $1.6 < |\eta| < 2.2$  in the face of high luminosity [27]. The project foresees the installation of 72-ten-degree chambers per endcap of CMS. For charged-particle detection, the GE1/1 muon upgrade employs gas electron multipliers (GEMs). GEMs exploit electron amplification that occurs within a gas medium inside narrow holes that perforate a thin polyimide foil in a hexagonal pattern. The GEM foil is clad on both sides with thin conductive layers of copper. A voltage of a few hundred volts is applied across the two layers which creates a strong electric field (60-100 kV/cm) inside the holes that causes electron-ion avalanches in the gas. An arrangement of three cascaded GEM foils, commonly known as a ?Triple-GEM detector? (Figure 2.19) is currently used.

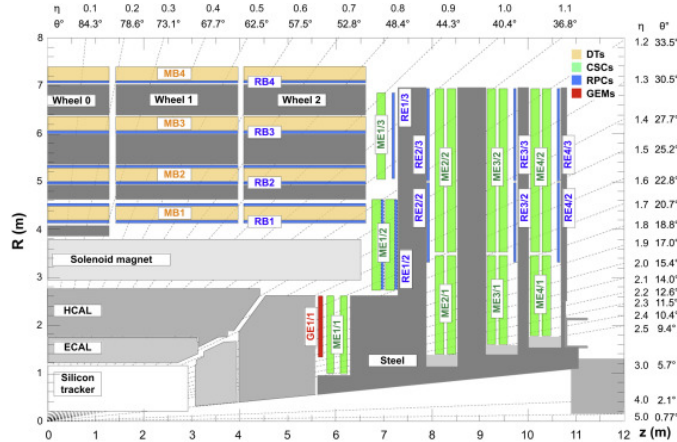


Figure 2.18: A quadrant of the R - z cross-section of the CMS detector, highlighting in red the location of the proposed GE1/1 detector within the CMS muon system.

## 2.5 Trigger and Data Acquisition

The trigger system in CMS is the start of the physics event selection process. A decision to retain an event for further consideration has to be made every 25 ns. This decision is based on the event's suitability for inclusion in one of the various datasets to be used for analysis. The datasets to be taken are determined by CMS physics priorities as a whole. These datasets include dilepton and multilepton datasets, diphoton datasets,

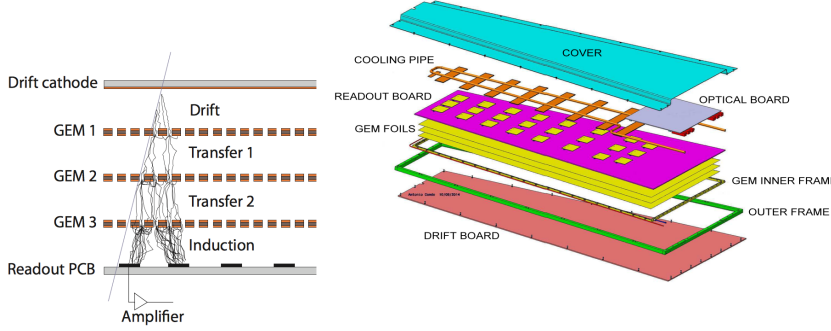


Figure 2.19: Left: By cascading three GEM foils, the amplification per stage can be kept modest to avoid electric breakdown problems. Right: Exploded view of the mechanical design of a Triple-GEM chamber.

lepton plus jet datasets for top, Higgs and BSM physics, and inclusive electron datasets for calorimeter calibrations. In addition, other samples are necessary for measuring efficiencies in event selection and studying backgrounds. The trigger has to select these samples in real time along with the main data samples. For the nominal LHC design luminosity of  $10^{34} \text{ cm}^{-2} \text{s}^{-1}$ , an average of 17 events occurs at the beam crossing frequency of 25 ns. This input rate of  $10^9$  interactions every second must be reduced by a factor of at least  $10^7$  to 100 Hz, the maximum rate that can be archived by the on-line computer farm. CMS has chosen to reduce this rate in two steps. At the first level (L1 [28]) all data is stored for  $3.2 \mu\text{s}$ , after which no more than 100 kHz of the stored events are forwarded to the High Level Triggers (HLT). The L1 system uses only coarsely segmented data from calorimeter and muon detectors, while holding all the high-resolution data in pipeline memories in the front-end electronics. The HLT [29] is provided by a subset of the on-line processor farm which, in turn, passes a fraction of these events to the remainder of the on-line farm for more complete processing.

### 2.5.1 Level 1 Trigger

The design of the CMS Trigger and Data Acquisition system is illustrated in figure 2.20. At the first level all information about the event is preserved. The first level decision is made, with negligible dead-time, on a subset of the total information available for the events. Since signal propagation delays are included in this pipeline time, the L1 trigger calculations must be done in many cases in less than  $1 \mu\text{s}$ . If the first level trigger generates an accept, the event data are moved or assigned to a buffer for readout and processing by the High Level Triggers. The L1 trigger involves the calorimetry and muon systems as well as some correlation of information from these systems. The L1 decision is based on the presence of local objects such as photons, electrons, muons, and jets, using information from calorimeters, and muon systems in a given element of  $\eta$ - $\phi$  space. It also employs global sums of  $E_T$  and missing  $E_T$ . Each of these items is tested against several  $p_T$  or  $E_T$  thresholds.

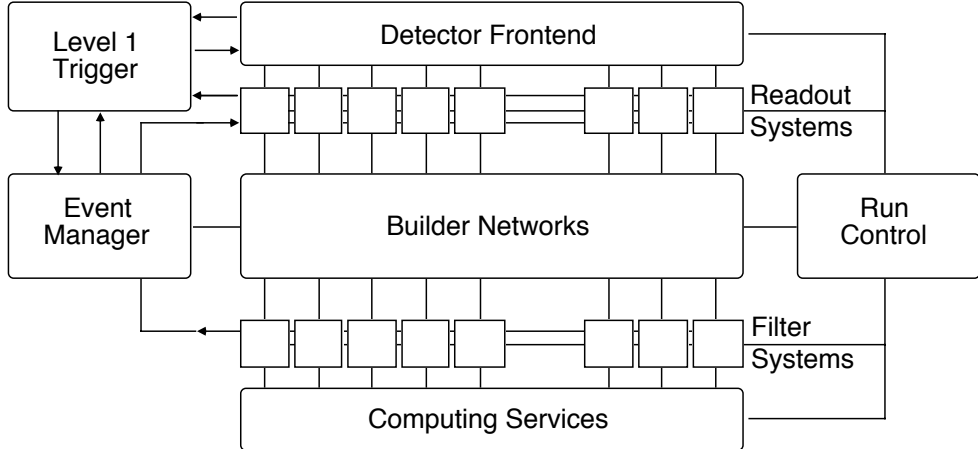


Figure 2.20: CMS Trigger and Data Acquisition System.

### High Level Trigger

The CMS Level-1 Trigger System is required to reduce the input interaction rate of 1 GHz to a filtered event rate of 75 kHz. To match the capabilities of the mass storage and offline computing systems, the final output of the experiment should not exceed 100 events per second. The High Level Triggers have access to all the information used in L1 since this is stored locally in the L1 trigger crates. Consequently, High Level Triggers can make further combinations and other topological calculations on the digital list of objects transmitted from L1. Eventually, the High Level Triggers use the full event data for the decision to keep an event.



## Chapter 3

# Object reconstruction in CMS

The global event reconstruction (also called particle-flow event reconstruction [30]) aims to reconstruct and identify each individual particle in an event, with an optimized combination of all subdetector information, Figure 3.1. In this process, the identification of the particle type (photon, electron, muon, charged hadron, neutral hadron) plays an important role in the determination of the particle direction and energy. Photons (e.g. coming from  $\pi^0$  decays or from electron bremsstrahlung) are identified as ECAL energy clusters not linked to the extrapolation of any charged particle trajectory to the ECAL. Electrons are identified as a primary charged particle track and potentially many ECAL energy clusters corresponding to this track extrapolation to the ECAL and to possible bremsstrahlung photons emitted along the way through the tracker material. Muons are identified as a track in the central tracker consistent with either a track or several hits in the muon system, associated with an energy deficit in the calorimeters. Charged hadrons are identified as charged particle tracks neither identified as electrons, nor as muons. Finally, neutral hadrons are identified as HCAL energy clusters not linked to any charged hadron trajectory, or as ECAL and HCAL energy excesses with respect to the expected charged hadron energy deposit.

### 3.1 Photons

Photons [32] for use as signals or signatures in measurements and searches, rather than for use in the construction of jets or missing transverse energy, are reconstructed from energy deposits in the ECAL using algorithms that constrain the clusters to the size and shape expected for electrons and photons with  $p_T \geq 15$  GeV. The algorithms do not use any hypothesis as to whether the particle originating from the interaction point is a photon or an electron, consequently electrons from  $Z \rightarrow e^+e^-$  events, for which pure samples with a well defined invariant mass can be selected, can provide excellent measurements of the photon trigger, reconstruction, and identification efficiencies, and of the photon energy scale and resolution. The reconstructed showers are generally limited to a fiducial region excluding the last two crystals at each end of the barrel ( $|\eta| < 1.4442$ ). The outer circumferences of the endcaps are obscured by services passing between the

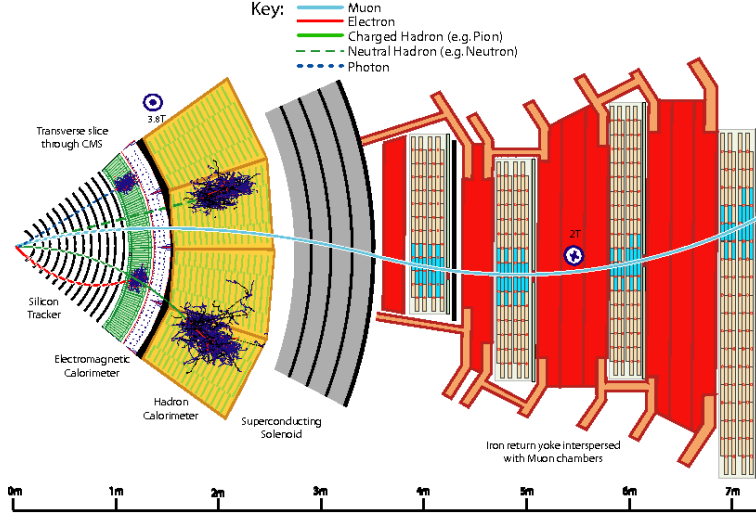


Figure 3.1: Particle interaction and reconstruction in a transverse slice of the CMS detector, from the beam pipe to the muon detector.

barrel and the endcaps, and this area is removed from the fiducial region by excluding the first ring of trigger towers of the endcaps ( $|\eta| > 1.566$ ). The fiducial region terminates at  $|\eta| = 2.5$  where the tracker coverage ends. The photon reconstruction proceeds through several steps:

- calibration: the calorimeter signals in data must be calibrated and corrected for several detector effects
- clusterisation: clustering algorithms collect the energy from radiating electrons and converted photons that gets spread in the  $\phi$  direction by the magnetic field; these algorithms are evolved from fixed matrices of  $5 \times 5$  crystals, which provide the best reconstruction of unconverted photons, by allowing extension of the energy collection in the  $\phi$  direction, to form "superclusters"
- correction of cluster energy: main effects (e.g. variation of longitudinal containment, variation of lateral containment or variation in the amount of energy absorbed before reaching the ECAL for showers starting before the ECAL) force to correct the initial sum of energy deposits

## 3.2 Electrons

Electrons [33] are reconstructed by associating a track reconstructed in the silicon detector with a cluster of energy in the ECAL. A mixture of a stand-alone approach [34] and the complementary global particle-flow algorithm is used to maximize the performance. The electron energy usually spreads out over several crystals of the ECAL. This spread

can be quite small when electrons lose little energy via bremsstrahlung before reaching ECAL. To measure the initial energy of the electron accurately, it is essential to collect the energy of the radiated photons that mainly spreads along the  $\phi$  direction because of the bending of the electron trajectory in the magnetic field. The spread in the  $\eta$  direction is usually negligible, except for very low  $p_T$  ( $p_T < 5\text{GeV}$ ). Two clustering algorithms, the "hybrid?" algorithm in the barrel, and the "multi-5x5" in the endcaps, are used for this purpose.

The starting point of the hybrid algorithm is a seed crystal, defined as the one containing most of the energy deposited in any considered region: arrays of  $5 \times 1$  crystals in  $\eta \times \phi$  are added around the seed crystal, in a range of  $N_{steps}$  crystals in both directions of  $\phi$  if their energies exceed a minimum threshold. The contiguous arrays are grouped array into clusters, with each distinct cluster required to have a seed array with energy greater than a threshold in order to be collected in the final global cluster, called the supercluster seed-array (SC).



# Bibliography

- [1] C. Patrignani et al. *Particle Data Group*, Chin. Phys. C, 40, 100001 (2016) and 2017 update.
- [2] Halzen and Martin, *Quarks and Leptons: An Introductory Course in Modern Particle Physics*, John Wiley & Sons (1984).
- [3] M.E.Peskin and D.V.Schroeder, *An Introduction To Quantum Field Theory*, Addison-Wesley, 1995.
- [4] M.Maggiore, *A Modern Introduction to Quantum Filed Theory*, Oxford University Press, 2004.
- [5] A.Pich, *The standard model of electroweak interactions*, arXiv:hep-ph/0502010v, 2005.
- [6] UA1 Collaboration, *Experimental observation of isolated large transverse energy electrons with associated missing energy at  $\sqrt{s}=540$  GeV*.
- [7] UA1 Collaboration, *Experimental observation of lepton pairs of invariant mass around  $95$   $GeV/c^2$  at the CERN SPS collider*.
- [8] S. Weinberg, *A model of leptons*, Phys. Rev. Lett. 19 (1967) 1264.
- [9] MuLan Collaboration, *Improved Measurement of the Positive Muon Lifetime and Determination of the Fermi Constant*, Phys.Rev.Lett.99:032001,2007, arXiv:0704.1981.
- [10] J.M. Cornwall, D.N. Levin, and G. Tiktopoulos, Phys. Rev. Lett. 30, 1286 (1973) and Phys. Rev. D10, 1145 (1974);  
C.H. Llewellyn Smith, Phys. Lett. B46, 233 (1973).
- [11] B.W. Lee, C. Quigg, and H.B. Thacker, Phys. Rev. D16, 1519 (1977).
- [12] ATLAS Collaboration, *Observation of a new particle in the search for the Standard Model Higgs boson with the ATLAS detector at the LHC*, Phys.Lett. B716 (2012), pp. 1-29, DOI: 10.1016/j.physletb.2012.08.020.

- [13] CMS Collaboration, *Observation of a new boson at a mass of 125 GeV with the CMS experiment at the LHC*, Physics Letters B716 (2012), pp. 30-61. DOI: <http://dx.DOI.org/10.1016/j.physletb.2012.08.021> .
- [14] LHC Higgs Cross Section Working Group, <https://twiki.cern.ch/twiki/bin/view/LHCPhysics/LHCHXSWG>.
- [15] D. de Florian et al., *LHC Higgs Cross Section Working Group*, CERN-2017-002-M, arXiv:1610.07922[hep-ph] (2016).
- [16] CMS Collaboration, *Observation of  $t\bar{t}H$  production*, arXiv:1804.02610 [hep-ex] (2018)
- [17] S. Heinemeyer et al., *LHC Higgs Cross Section Working Group*, CERN?2013?004, arXiv:1307.1347 [hep-ph] (2013).
- [18] D. de Florian et al., *LHC Higgs Cross Section Working Group*, CERN?2017?002-M, arXiv:1610.07922[hep-ph] (2016).
- [19] Lyndon Evans and Philip Bryant, *LHC Machine*, 1748-0221-3-08-S08001, Journal of Instrumentation (2008), <http://stacks.iop.org/1748-0221/3/i=08/a=S08001>
- [20] CMS Collaboration, *The Compact Muon Solenoid technical proposal*, CERN-LHCC-94-38, <http://cdsweb.cern.ch/record/290969>
- [21] CMS Collaboration, *The CMS tracker system project: technical design report*, CERN-LHCC-98-006, <http://cdsweb.cern.ch/record/368412>.
- [22] CMS Collaboration, *The CMS tracker: addendum to the technical design report* CERN-LHCC-2000-016, <http://cdsweb.cern.ch/record/490194>.
- [23] Anirban Saha, *Phase 1 upgrade of the CMS pixel detector*, Journal of Instrumentation (2017), <http://stacks.iop.org/1748-0221/12/i=02>
- [24] PARTICLE DATA GROUP Collaboration, S. Eidelman et al., *Review of particle physics* Phys. Lett. B 592 (2004) 1.
- [25] CMS Collaboration, *The hadron calorimeter project: technical design report*, CERN-LHCC-97-031, <http://cdsweb.cern.ch/record/357153>.
- [26] CMS Collaboration, *The CMS muon project, technical design report*, CERN-LHCC-97-032, <http://cdsweb.cern.ch/record/343814>.
- [27] CMS Collaboration, *CMS TECHNICAL DESIGN REPORT FOR THE MUON ENDCAP GEM UPGRADE*, CERN-LHCC-2015-012, <https://cds.cern.ch/record/2021453/files/CMS-TDR-013.pdf>
- [28] CMS Collaboration, *CMS. The TriDAS project. Technical design report, vol. 1: The trigger systems*. In: (2000).

- [29] CMS Collaboration, *CMS The TriDAS Project: Technical Design Report, Volume 2: Data Acquisition and High-Level Trigger. CMS trigger and data-acquisition project. Technical Design Report CMS*. Geneva: CERN, 2002. url: <http://cds.cern.ch/record/578006>.
- [30] Sirunyan, A. M. and others, *Particle-flow reconstruction and global event description with the CMS detector*, JINST, 12, 2017, P10003, 10.1088/1748-0221/12/10/P10003
- [31] , Cacciari, Matteo and Salam, Gavin P. and Soyez, Gregory, *The anti- $k_t$  jet clustering algorithm*, JHEP, 04, 2008, 063, 10.1088/1126-6708/2008/04/063
- [32] Khachatryan, Vardan and others, *Performance of photon reconstruction and identification with the CMS detector in proton-proton collisions at  $\sqrt{s} = 8$  TeV*, JINST, 10, 2015, P08010, 10.1088/1748-0221/10/08/P08010, 1502.02702
- [33] Khachatryan, Vardan and others, *Performance of electron reconstruction and selection with the CMS detector in proton-proton collisions at  $\sqrt{s} = 8$  TeV*, JINST, 10, 2015, P06005, 10.1088/1748-0221/10/06/P06005, 1502.02701
- [34] S. Baffioni et al., *Electron reconstruction in CMS*, Eur. Phys. J. C 49 (2007) 1099, doi:10.1140/epjc/s10052-006-0175-5.

